

Type II supernovae Early Light Curves

Tomer Shussman^{1*}, Roni Waldman^{2,3} and Ehud Nakar¹

¹*The Raymond and Beverly Sackler School of Physics and Astronomy, Tel Aviv University, Tel Aviv 69978, Israel*

²*Racah Institute of Physics, The Hebrew University, Jerusalem 91904, Israel*

³*Particle Physics & Astrophysics Dept., Weizmann Institute of Science, Rehovot 76100, Israel*

Last updated 19 October 2016

ABSTRACT

Observations of type II supernova early light, from breakout until recombination, can be used to constrain the explosion energy and progenitor properties. Currently available for this purpose are purely analytic models, which are accurate only to within an order of magnitude, and detailed numerical simulations, which are more accurate but are applied to any event separately. In this paper we derive an analytic model that is calibrated by numerical simulations. This model is much more accurate than previous analytic models, yet it is as simple to use. To derive the model we analyze simulated light curves from numerical explosion of 124 red supergiant progenitors, calculated using the stellar evolution code MESA. We find that although the structure of the progenitors we consider varies, the resulting light curves can be described rather well based only on the explosion energy, ejecta mass and progenitor radius. Our calibrated analytic model, which is based on these three parameters, reproduces the bolometric luminosity within 25% – 35% accuracy and the observed temperature within 15% accuracy (compared to previous analytic models which are indeed found to be accurate only to within an order of magnitude). We also consider deviations of the early time spectrum from blackbody, and find that the Rayleigh-Jeans regime is slightly shallower (roughly $L_\nu \propto \nu^{1.4}$). This modified spectrum affects the optical/near-UV light curve mostly during the first day when the typical observed temperature is $\gg 10^4$ °K. We use our results to study the optical and near-UV early light curves from first light until recombination and briefly discuss what can be learned from current and future observations. Light curves generated using our calibrated model can be downloaded at <http://www.astro.tau.ac.il/~tomersh/>.

1 INTRODUCTION

Type II-P and possibly also type II-L supernova (SN) are generated by the explosion of red supergiants (RSGs) (Smartt 2009). In these progenitors, the core collapse generates a shock which propagates through the hydrogen-rich envelope. As the shock reaches the stellar surface, first light is emitted (Colgate 1974; Falk 1978; Imshennik et al. 1981; Ensmann & Burrows 1992; Matzner & McKee 1999). After the shock breaks out of the star, the envelope radiates as it expands, leading to a long lasting emission that decays slowly (Grassberg et al. 1971; Chevalier 1976, 1992; Tominaga et al. 2009; Piro et al. 2010; Nakar & Sari 2010; Rabinak & Waxman 2011; Dessart et al. 2013).

Observations of type II SN light curves can be used to constrain the stellar properties and explosion energy, and shed light on the inner structure of RSG progenitors. Observations at early times (until about 10 days after the breakout) may be especially useful since the physics at these times is relatively “clean” from recombination, line emission, and radioactive decay, as pure hydrodynamic and radiation transport in ionized hydrogen govern the evolution and emission. In addition, early observations can provide independent constraints on the explosion and progenitor param-

eters. Finally, the emission at early times allows for probing the outer parts of the progenitor ($10^{-3} - 10^{-1} M_\odot$) which are otherwise hardly accessible. During the last decade, growing numbers of type II SNe early light curves became available (e.g., Gezari et al. 2008; Schawinski et al. 2008; Arcavi et al. 2012; Anderson et al. 2014; Faran et al. 2014; Sanders et al. 2015; González-Gaitán et al. 2015; Gall et al. 2015; Rubin et al. 2015). In the near future, we expect that multi-wavelength observations of the early emission will be widely available. Inspired by the possibility of future observations, we revisit the subject.

Previous studies of the light curve generated by a shock breakout and cooling envelope emission at early times were either based on numerical calculations of specific progenitors (e.g., Shigeyama et al. 1988; Woosley 1988; Ensmann & Burrows 1992; Blinnikov et al. 1998; Schawinski et al. 2008; Tominaga et al. 2009, 2011; Dessart et al. 2013; Morozova et al. 2016) or on using analytic models (e.g., Weaver 1976; Chevalier 1992; Matzner & McKee 1999; Piro et al. 2010; Katz et al. 2010; Sapir et al. 2011; Sapir & Waxman 2016), in which a specific (“analytic”) progenitor profile was assumed. Recently, Nakar & Sari (2010) [NS10] and Rabinak & Waxman (2011)

arXiv:1610.05323v1 [astro-ph.HE] 17 Oct 2016

[RW11] proposed analytic models to describe the bolometric luminosity and observed temperature of RSG progenitors from first light to about 10 days.

The main advantage of the analytic models is that they provide global relations between the observables and the explosion and progenitor properties, which can be easily applied to large data sets, such as the ones that have recently begun accumulating. In addition, the models enable predictions of the signal based on the progenitor properties, for the planning of future observations. Finally, the use of analytic relations enhances the understanding of the underlying physical mechanisms. However, these models are limited by the need to make many approximations on the stellar structure, the dynamics of the problem and the radiation transfer. The result of these approximations is that the analytic models are accurate only to within an order of magnitude. Numerical models, on the other hand, require less assumptions and are therefore more accurate, but so far they were used to study specific SNe or to generate light curves for a set of progenitors, without providing a general model for the effect of each parameter on the early light curve.

The goal of this paper is to provide an analytic model, with all of its advantages, that is accurate at a level close to that of numerical simulations. For that we numerically simulate the explosions from a large set of progenitors, and combine the results with analytic understanding of the light curve evolution, in order to construct a calibrated analytic model that is simple, yet accurate, and can be used to analyze large data sets in the future.

In order to do so, we separate the problem into two stages. First, we calculate numerically the light curves generated by exploding progenitors with the same density profile, but with different explosion energies, and progenitor radii and masses. We consider an analytic progenitor prototype with a structure similar near the stellar edge to that assumed in previous analytic studies (e.g., NS10, RW11), but more realistic in inner parts of the star. For these progenitors, the effect of each progenitor and explosion property on the light-curve is extracted for a wide range of values, independently of other properties. Since the early emission depends mostly on the conditions at the breakout in the outer parts of the progenitor, and not directly on the total explosion energy and ejecta mass, we find the dependence of the light curve on properties of the breakout (e.g., breakout velocity, density at the breakout location, etc.). We also find a mapping between the breakout parameters and the global ones (explosion energy, ejecta mass and progenitor radius) to obtain the dependence of the light curve on these parameters. Second, we use a large set of more than a 100 RSG progenitors, calculated using the stellar evolution code MESA, to study the effect of different, more realistic structures on the emission. Here we also find the dependence of the light curve on the breakout parameters and then use them to find the dependence on the global SN parameters. Despite the large set of numerically calculated progenitors, their features are limited to the range of progenitor parameter space that we study and the specific schemes used in the stellar evolution simulations. Therefore the relations obtained based on this set are more accurate but are specific in part for the progenitors we checked. We discuss which of our results are more general and which depends more strongly on the exact progenitor structures. We also pay special at-

tention to the deviation of the observed spectrum from a blackbody in the Rayleigh-Jeans regime and construct an analytic approximation of the observed spectrum.

The paper proceeds as follows: A brief review of the theory developed in previous analytic studies is presented in section 2. In section 3 we obtain relations between progenitor and explosion properties and the bolometric luminosity and observed temperature for an analytic star. We show where earlier analytic models are accurate, where they fail and why. Results for numerically calculated stars are shown and discussed in section 4, where the effects of deviation of the observed spectrum from a blackbody and of light travel time are also studied. In section 5 we summarize the model which relates the light-curve to the breakout and progenitor properties. A reader that is interested only in the final scaling relations should refer to this section. An analysis of the optical light curve appears in section 6, and an analysis of the velocity of the photosphere appears in section 7. Our main conclusions are summarized in section 8.

2 THEORY

SN explosion drives a radiation dominated shock that propagates through the decreasing density profile of the stellar envelope. At first (after the shock crosses envelope mass that is comparable to the He core mass), the dynamics of the problem are similar to the Sedov-Taylor (Taylor 1950; Sedov 1959) explosion, but as the shock reaches the edge of the star, it accelerates because of the steep density decrease. A hydrodynamic solution for shock acceleration was proposed by Sakurai (1960), for a density profile $\rho \propto (R_* - r)^n$ where R_* is the progenitor radius, r is the distance from the center and n is a parameter which is usually assumed to equal $n = 1.5$ for a RSG. This solution is planar and is therefore applicable only to the stellar edge, namely, $R_* - r \ll R_*$. Being mediated by radiation, the shock has a width of optical depth $\tau_s \simeq c/v_s(r) \simeq c/v(r)$ (Weaver 1976), where c is the speed of light and $v_s(r)$ [$v(r)$] is the shock [matter just behind the shock] velocity. The shock keeps accelerating up to the point at which the optical depth for photons to escape the envelope $\tau(r)$ becomes comparable to τ_s . At this point, the shock "breaks-out" of the star, and first radiation is emitted. After the breakout, the envelope keeps radiating as it expands. During the expansion, a rarefaction wave propagates inwards and the velocity of the outer layers of the envelope roughly doubles itself. A model that describes the hydrodynamic expansion of the envelope is presented by Matzner & McKee (1999).

The hydrodynamic evolution of the expansion has two phases - a planar phase, which occurs at early times, when the expanding gas radius has not yet doubled its initial radius, and a spherical phase which begins approximately when the radius is doubled. The nature of the emitted radiation changes significantly between the phases. During the planar phase τ of each mass element is constant while the diffusion time from each element grows linearly in time, similarly to the dynamical time. Therefore during this phase radiation escapes only from the same mass shell from which radiation escaped at the breakout (NS10, Piro et al. 2010). Following NS10, we denote this shell the breakout shell, and note that it obeys $\tau \simeq c/v_s$ at the breakout. During the

spherical phase, however, τ of each mass element decreases with time, and inner shells begin to dominate the emitted radiation. Through the entire evolution (from breakout and up to recombination) the observed luminosity is generated at the shell that satisfies $\tau \approx c/v$. This shell is denoted (following NS10) as the luminosity shell.

During the expansion the envelope cools down rapidly because of adiabatic and radiation losses. At around $t \approx 10 - 20$ days after the breakout, the observed temperature reaches $T \approx 7500^\circ\text{K}$, and recombination of hydrogen atoms becomes significant. The recombination yields a rapid opacity drop which affects the observed temperature and luminosity. In addition, at times earlier than $t \approx 10 - 20$ days, the contribution of deposited energy by ^{56}Ni radioactive decay to the light curve is negligible.

In this work, we focus on calculating the emitted radiation at early times, when the temperature is high enough for the hydrogen to be fully ionized and ^{56}Ni radioactive decay is negligible. For these times, NS10 obtained an analytic estimate of the emitted radiation at the breakout, and the planar and spherical phases. In order to do that, they used the following approximations and assumptions:

Assum. 1 The explosion is fully spherical, and therefore the evolution is one dimensional.

Approx. 2 Energy deposition by ^{56}Ni radioactive decay is negligible.

Approx. 3 Radiation transport is treated in the diffusion approximation. This is justified since both the luminosity and the observed temperature are determined at optical depth $\tau > 1$.

Approx. 4 When enough photons can be generated to maintain thermal equilibrium, the spectrum is assumed to be a blackbody.

Approx. 5 The diffusion opacity is dominated by Thomson scattering (e.g. over absorption processes) of fully ionized hydrogen and helium with primordial ratios, and the absorption opacity, which is used to determine the observed temperature, is dominated by free-free absorption (e.g. over bound-free and bound-bound transitions).

Approx. 6 The progenitor density profile near the edge is of a power law form with $n = 1.5$. (which is typical for RSG progenitors).

Assum. 7 The emission is always determined by shells near to the edge, namely, with initial (pre-explosion) coordinates $R_* - r \ll R_*$.

Assum. 8 The breakout shell structure during the expansion is of a simple planar rarefaction wave¹.

NS10 found that the bolometric luminosity consists of two power-laws, corresponding to the two phases of evolution. Defining t as the time relative to the bolometric peak emission, the luminosity scales as $t^{-\alpha}$ where $\alpha_p = 4/3$ for the planar stage, and $\alpha_s = 0.17$ for the spherical stage (equation 29 in NS10). The planar power law originates in the fact that only the breakout shell radiates during the planar stage, while its energy scales as $t^{-1/3}$ due to adiabatic

losses. Therefore, it is valid (up to a logarithmic factor) for every density profile in which the shock accelerates before the breakout. The spherical power law is determined by two factors: adiabatic losses, and the fact that inner shells radiate at later times. Its value is weakly dependent on n .

The rise-time, which is also the time it takes the planar phase to begin is $t_0 \approx d_0/v_0$ and the transition time between the planar and spherical power laws is $t_s \approx R_*/v_0$, where d_0 is the breakout shell's initial width, and v_0 is the matter velocity at breakout. The subscript '0' denotes the breakout shell mass (Lagrangian) coordinate. The bolometric luminosity at the breakout is $L_0 = E_0/t_0$ where $E_0 \approx \rho_0 v_0^2 4\pi R^2 d_0$ is the energy contained within the breakout shell at breakout, ρ_0 is the initial density at the breakout shell.

Assuming that the flux is well approximated by blackbody radiation, its temperature is determined at the last point from which enough photons can be generated to maintain thermal equilibrium. A measure of the thermal coupling is

$$\eta(m, t) \equiv \frac{n_{\text{BB}}}{\dot{n}t_{\text{d}}}, \quad (1)$$

where n_{BB} is the photons number density in the shell (assuming it is in thermal equilibrium), \dot{n} is the rate of photons emission in the shell (proportional to the absorption opacity via Kirchhoff's law of thermal radiation) and t_{d} is the diffusion time. At all times, $\eta(m)$ is monotonically decreasing with m measured from the edge of the star. Shells with $\eta > 1$ do not produce enough photons to maintain thermal equilibrium, while shells with $\eta < 1$ do, therefore the observed temperature is the temperature of the outermost shell which satisfies $\eta = 1$. If at the time of breakout this shell is inner to the breakout shell (also the point where the observed flux is determined), the breakout is out of thermal equilibrium and thermal equilibrium is obtained only during the spherical phase. If, on the other hand, this shell is outer to the breakout shell, thermal equilibrium is maintained at all times, starting from the breakout.

Most RSG explosions are found to be in thermal equilibrium from the breakout on, and the temperature scales with $t^{-\beta}$ where $\beta_p = 0.36$ and $\beta_s = 0.56$ (equation 31 in NS10). The observed temperature at the peak of bolometric luminosity is $T_{\text{obs},0} \approx T_{\text{BB},0}\eta_0^{0.14}$, where $T_{\text{BB},0} \approx (\rho_0 v_0^2 / a_{\text{BB}})^{1/4}$ is the temperature of the breakout shell at the time of the breakout, a_{BB} is the radiation constant, and η_0 is the value of η in the breakout shell at the breakout time. Both $T_{\text{BB},0}$ and η_0 are mainly dependent on v_0 (equations 16,18 in NS10). Note that since the temperature is not necessarily determined at the breakout shell, the observed temperature is different from the breakout shell temperature.

NS10 also derived the dependency of the breakout shell parameters (v_0 , ρ_0 , d_0 , η_0 , etc.) on the progenitor properties, namely R_* , the progenitor's radius, M_{ej} the ejecta mass, and E_{exp} the explosion energy (see appendix A, equations A-6, A-7, A-10, A-14 in NS10)². Substituting this dependency into the model to describe the emission, yields relations between the emission properties and the progenitor properties.

¹ Prior to the breakout, the evolution is governed by hydrodynamics alone, everywhere except for the breakout shell, where radiation transfer is important. Therefore, it is harder to describe it analytically.

² It is worth to note that d_0 is fully dependent on v_0 and ρ_0 , since $\tau_0 \approx c/v_0$ where $\tau_0 \approx [1/(n+1)]\kappa_T \rho_0 d_0$ is the optical depth of the breakout shell and κ_T is Thomson scattering opacity.

A similar analysis has been done by RW11, and [Chevalier \(1992\)](#), who obtained analytic estimates for the spherical phase only, and by [Piro et al. \(2010\)](#) who obtained estimates for both phases but for breakouts from white dwarf progenitors only. All the analytic models assumed similar progenitor structures, and obtained similar temporal power-law indices for the bolometric luminosity. The numerical coefficients of the light curve features vary by a factor of 2–4 between the studies. The temporal evolution of the temperature is a bit different between NS10 and the other studies, since only NS10 considered the thermal coupling in detail. [Sapir et al. \(2011\)](#) performed numerical calculations of the light curve at planar geometry, for a progenitor of $n = 1.5$, and found that the value of $L_0 = E_0/t_0$, as predicted by NS10, should be multiplied by a factor of 2. The rest of the estimates given above have not yet been checked numerically, especially for the spherical phase light curve, and using a more realistic progenitor structure.

3 NUMERICAL LIGHT CURVES OF ANALYTIC PROGENITORS

The analytic models described in section 2 are limited in the manner that they require rough assumptions on the dynamics of the problem and on the initial conditions. Specifically, approximation 6 is inaccurate for realistic progenitors, and progenitors with different stellar structures might yield different hydrodynamic evolution leading to different light curves. Due to assumption 7, the analytic models inherently ignore the hydrodynamics of the inner envelope, and their effect on the light curve. A correction is required at times late enough for the inner envelope to dominate the emission, which may take place before recombination has begun. Assumption 8 does not affect the bolometric luminosity, which is independent of the breakout shell structure, but could affect the evolution of the observed temperature. Finally, even within the limit of validity of the analytic models their predicted luminosity and observed temperature are only correct to within an order of magnitude.

When coming to obtain a better analytic approximation it is useful to separate properties of the light curve which are more general form properties that depend more strongly on the exact progenitor structure. Therefore, we do not start by studying numerically calculated progenitors, each with a different density profile. Instead, in this section we study the emission from a set of analytic progenitors, all of which have the same density distribution but different masses and radii. The definition of an analytic progenitor allows us also to easily study the effect of each parameter (e.g., R_* , M_{ej}) on the light-curve independently, and for a wide range of values. The density profile of the analytic progenitors that we consider is more realistic than the single power-law assumed in analytic calculations. It is a smooth connection of two power-laws, one from the center of the star ($\rho \propto r^{-k}$) and one from the edge of the star ($\rho \propto (R_* - r)^n$). Thus, in this section we relax assumptions 6–8 and study the effect of various values of R_* , M_{ej} and E_{exp} on the light curve. Since the emission at the breakout and during the planar phase depends only on the conditions at the breakout shell we also find a relation between the breakout shell param-

eters and the observed light curve (and between the breakout parameters and R_* , M_{ej} and E_{exp}).

In order to simulate the explosion, we wrote a 1D spherical geometry, two-temperatures Lagrangian computer program and used it to calculate the shock propagation and emitted radiation after the shock breakout. Gravitation is neglected because $GM_{ej}^2/R_* \ll E_{exp}$, and effects such as nucleosynthesis or energy deposition due to ^{56}Ni decay are neglected since they do not affect the light curve at early times. Therefore, our code solves the radiation hydrodynamic equations alone, under the diffusion approximation, thus keeping assumption 1 and approximations 2–3. In appendix A, we describe the code in detail and show its results for standard test cases.

For the equation of state (EOS) of the matter, we chose that of an ideal gas, with $\gamma = 5/3$, suitable for mono-atomic gas, and $\mu = 0.6$ which corresponds to a fully ionized mixture of hydrogen and helium with primordial ratios. Radiation is approximated as an ideal gas with $\gamma = 4/3$. The diffusion opacity includes Thomson scattering term, $\kappa_T = 0.34 \text{ cm}^2/\text{g}$, which corresponds to fully ionized hydrogen and helium with primordial ratios, in addition to an analytic estimation ([Zel'dovich & Raizer 1967](#)) of the absorption opacity from hydrogen free-free and bound-free interactions (this term is usually smaller than κ_T). This absorption opacity is also used to calculate the observed temperature (by post-processing). The opacities we use are appropriate as long as the hydrogen is completely ionized. Therefore, our solution is limited for temperatures higher than $T \approx 7500^\circ\text{K}$.

The observed temperature is calculated by post processing the hydrodynamic profiles. At each time, the observed temperature, T_{obs} , is defined as the temperature at the outermost point of the ejecta which is in thermal equilibrium. NS10 denote this point "color shell", while in other works it is denoted "thermalization depth". This definition of the observed temperature is applicable as long as the luminosity shell is in thermal equilibrium (see conditions for that in sub-section 4.5). As discussed in section 2, at the color shell $\eta = 1$, which is equivalent to the condition $\tau_{abs}\tau = 1/3$, where $\tau_{abs}(m)$ is the Planck mean absorption optical depth from coordinate m to the observer and $\tau(m)$ is the total diffusion optical depth (dominated by scattering). Thus, for each time-step we find the point where $\tau_{abs}\tau = 1/3$, and define T_{obs} as the temperature at this location³.

By including hydrogen bound-free interactions, our work further expands the analytic work of NS10, which only included hydrogen free-free interactions for the temperature determination (approximation 5). The effect of bound-free opacity on the thermal coupling and observed temperature is discussed in appendix B, which also includes a comparison between the opacity of pure hydrogen, hydrogen and helium with primordial ratios, and solar metallicity. We find that in the temperatures and densities of interest, helium and metal bound-free transitions are negligible compared to hydrogen free-free and bound-free transitions, and therefore our choice of opacity describes the thermal coupling well.

³ We verify that T_{obs} is not very sensitive to the exact definition, e.g., choosing a different numerical value for the thermalization condition, such as $\tau_{abs}\tau_s = 1$ yields around 5% difference in the observed temperature.

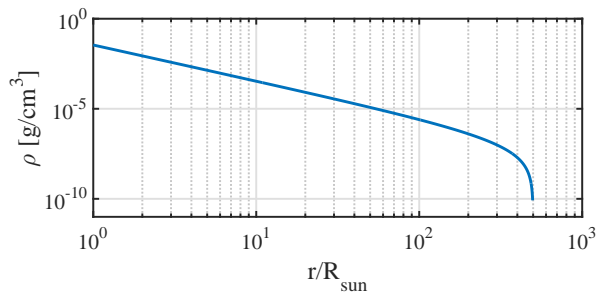


Figure 1. The analytic progenitor prototype density profile. The profile is composed of two power laws, one of the distance from the center and one of the distance from the edge (see text).

As an analytic progenitor, we use a prototype with density profile $\rho(r) = Kr^{-k}(R_* - r)^n$. This density profile is a more realistic estimation of the envelope density, than the single power law approximation discussed at section 2. We choose values of $k = 2$ and $n = 1.5$ which is a simple fit to the progenitors presented in Matzner & McKee (1999) and to the ones calculated for this work (see section 4). The value of K is determined by M_{ej} . An example of the structure, for a progenitor with $M_{\text{ej}} = 15M_{\odot}$, $R_* = 500R_{\odot}$ is shown in figure 1.

3.1 The breakout shell parameters as a function of the progenitor properties

The parameters of the breakout shell can be extracted from the code by looking at the hydrodynamic properties when $\tau \simeq c/v$. In order to be consistent, we defined the time of breakout at the point in which the velocity of the outermost mass element reached 1/3 of the maximal velocity at that time. We found that this corresponds to $\tau_0 = 1.2c/v_0$, and to the point in which the luminosity reached 1/2 of the maximal luminosity, for all the analytic progenitors. An example of the velocity profile near the envelope edge, for different times before and after the breakout is shown in figure 2. At the snapshot time of the dotted purple line, the luminosity is practically zero, while at the snapshot time of the dotted brown line, the luminosity has already reached its peak. Thus, any definition of the breakout time must be between the two times that the snapshots depicted in the two dotted lines were taken. It can be seen that the maximal velocity changes by 20% between the two dotted lines. Therefore, the definition of the breakout (the dashed black line) is robust, and the scaling relations obtained in this work are insensitive to the exact definition of the time of breakout.

Numerical calculations of the breakout were performed for progenitors of the same structure (See figure 1), with different radii, masses and explosion energies. The velocity, density and width of the breakout shell are found to scale within 1% (the expected numerical error) as

$$\rho_0^A = 6.3 \cdot 10^{-10} \text{ g/cm}^3 M_{15}^{0.67} R_{500}^{-1.64} E_{51}^{-0.31}, \quad (2a)$$

$$v_0^A = 5000 \text{ km/s} M_{15}^{-0.44} R_{500}^{-0.24} E_{51}^{0.56}, \quad (2b)$$

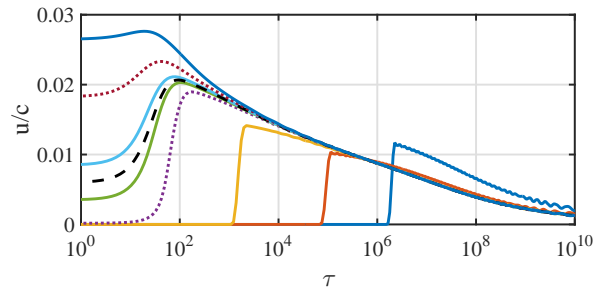


Figure 2. The velocity profile near the envelope edge at different times. τ is the diffusion optical depth to the observer. The breakout according to our definition is plotted in a black dashed line. The dotted lines mark the times where the luminosity rises from 10^{-4} of the peak (purple) to the peak (red).

$$\frac{d_0^A}{R_*} = 2 \cdot 10^{-2} M_{15}^{-0.21} R_{500}^{0.9} E_{51}^{-0.25}, \quad (2c)$$

where $M_x = M_{\text{ej}}/xM_{\odot}$, $R_x = R_*/xM_{\odot}$ and $E_x = E_{\text{exp}}/10^x \text{ erg}$. The superscript A notates the results for the analytic progenitors. We note that, as expected,

$$d_0 = \frac{2.5c}{\kappa_T \rho_0 v_0}. \quad (3)$$

The power law scaling relations are all similar to the ones defined in appendix A of NS10, but the numerical coefficients are different by factors ranging between 1.1 and 3. The breakout shell temperature is found to be

$$T_{\text{BB},0} = 1.2(\rho_0 v_0^2 / a_{\text{BB}})^{1/4} = 4.5 \cdot 10^5 \text{ }^\circ\text{K} M_{15}^{-0.05} R_{500}^{-0.53} E_{51}^{0.2}. \quad (4)$$

3.2 Bolometric light curve and observed temperature as functions of the breakout properties

Using the same progenitors, the scaling of the luminosity and observed temperature evolution with the breakout parameters can be found. From here on, we define the time that the bolometric luminosity peaks as $t = 0$. We focus first on the emission after the peak and ignore light travel time (namely we ignore the difference in arrival time of photons that are emitted at the same time but from different locations on the expanding sphere). A typical light curve obtained using the simulation is shown at the top of figure 3. It is best fit to a broken power law analytic formula with the form:

$$L_{\text{obs}}(t) \simeq L_0 \begin{cases} 1 & t \ll t_0 \\ \left(\frac{t}{t_0}\right)^{-4/3} & t_0 \ll t \ll t_s \\ \left(\frac{t_s}{t_0}\right)^{-4/3} \left(\frac{t}{t_s}\right)^{-0.35} & t_s \ll t \end{cases} \quad (5)$$

The best fit for the diffusion time at the breakout, planar to spherical transition time and maximal flux is:

$$t_0 = d_0/5v_0, \quad (6a)$$

$$t_s = R_*/6v_0, \quad (6b)$$

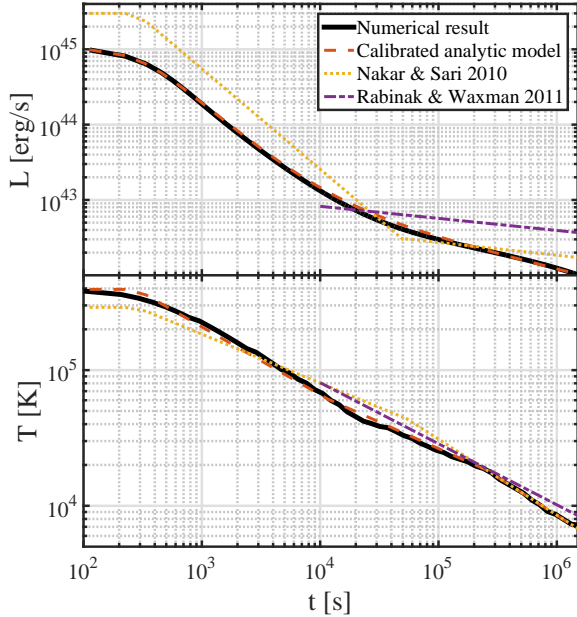


Figure 3. The bolometric luminosity and observed temperature of a typical analytic RSG progenitor. t is measured from the peak of the bolometric luminosity. Light travel time is ignored. The numerical result (solid black line) is compared to the calibrated analytic model (dashed red line), and to the analytic models of NS10 (dotted yellow line) and RW11 (dotted-dashed purple line). The progenitor and explosion properties are $M_{\text{ej}} = 15M_{\odot}$, $R_* = 500R_{\odot}$ and $E_{\text{exp}} = 10^{51}$ erg.

$$L_0 \equiv E_0/t_0 = 1.7\rho_0 v_0^3 2\pi R_*^2. \quad (6c)$$

The numerical coefficients for the transition times compared to the non-calibrated analytic prediction shows that the latter is indeed accurate only to within an order of magnitude. In order to improve the analytic approximation we use a smooth broken power law. At the transition between the planar and the spherical phases, the luminosity is well described by a sum of the planar and spherical luminosity, while at the transition between the breakout and the planar phase an harmonic sum of squares of the constant and planar luminosity is proper:

$$L_{\text{obs}}(t) = \begin{cases} (L_{t \ll t_0}^{-2} + L_{t_0 \ll t \ll t_s}^{-2})^{-0.5} & t \approx t_0 \\ L_{t_0 \ll t \ll t_s} + L_{t_s \ll t} & t \approx t_s \end{cases}. \quad (7)$$

As illustrated in figure 3, this model fits the numerical calculation to within 5% accuracy at all times. The planar phase luminosity power law of $\alpha_p = 4/3$ is the one predicted by the analytic models (see section 2). The spherical phase luminosity, however, is characterized by a decreasing power law $\alpha_s = 0.3 - 0.4$, which is more rapid than the predicted value of 0.17. The steeper decrease is due to the large radius of RSG progenitors, which yields a long planar - spherical transition time. For those progenitors, by the time the spherical phase has begun, the light curve is already dominated by inner parts of the envelope, where the density is not a pure power law and $(R_* - r)/R_* \sim 1$, so the analytic models

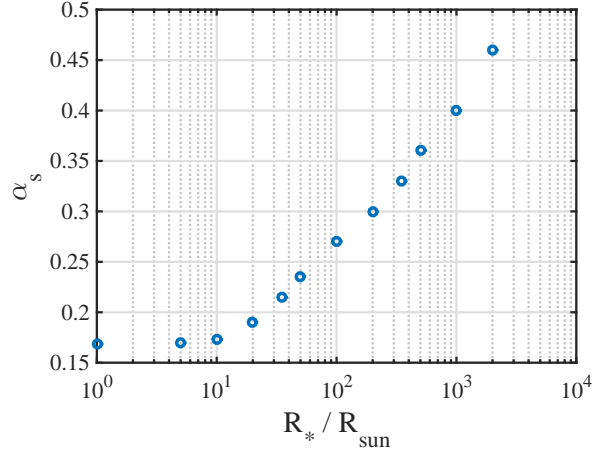


Figure 4. The temporal power law index for the spherical phase of the bolometric luminosity as calculated numerically for analytic progenitors with $M_{\text{ej}} = 15M_{\odot}$, $E_{\text{exp}} = 10^{51}$ erg and varying R_* . Progenitors with radii $R_* < 10R_{\odot}$ yield an index value 0.17 which is similar to the analytic model, but progenitors with $R_* \approx 500R_{\odot}$ (typical for RSG progenitors) yield a more rapid decrease.

fail to describe the emission accurately. Figure 4 shows the spherical temporal power law index as a function of R_* , obtained by calculations of progenitors with radii much smaller and larger than that of a typical RSG radius, $M_{\text{ej}} = 15M_{\odot}$ and $E_{\text{exp}} = 10^{51}$ erg. The spherical power in every calculation is obtained by best fitting the spherical emission to a power law until $t = 15$ d. As seen in figure 4, progenitors with $R_* < 10R_{\odot}$ yield a spherical light curve with a decay power law index of 0.17 as expected, but for larger progenitors the power law index increases slowly with the radius. For the typical radii range of RSGs it is between 0.3 and 0.4.

Substituting equations 2 into equations 6 yields direct relations between the progenitor properties and the light curve properties. The relations describe the light curve to within 5%. For comparison, results of the analytic models, as described in section 2 are also shown in figure 3. Equations 2-7, which are basically a calibrated version of the analytic results, provide a much more accurate description of the light curve.

The observed temperature which corresponds to the light curve calculation discussed above, is shown at the bottom of figure 3, and compared with the non calibrated analytic models. The temperature evolution is somewhat different than the analytic predictions. While the prediction of NS10 is characterized by two power laws, one for the planar phase and one for the spherical phase, the temperature is better characterized by three power laws, corresponding to three phases:

$$T_{\text{obs}}(t) \simeq T_{\text{BB},0} \eta_0^{0.07} \times \begin{cases} 1 & t < t_0 \\ \left(\frac{t}{t_0}\right)^{-0.45} & t_0 \leq t < t_s \\ \left(\frac{t_s}{t_0}\right)^{-0.45} \left(\frac{t}{t_s}\right)^{-0.35} & t_s \leq t < t_c \\ \left(\frac{t_s}{t_0}\right)^{-0.45} \left(\frac{t_s}{t_c}\right)^{-0.35} \left(\frac{t}{t_c}\right)^{-0.6} & t_c \leq t \end{cases}. \quad (8)$$

The temperature temporal evolution and the difference from NS10 predictions can be understood as follows. During the planar phase, the color shell is outer to the breakout shell (relative to the center of the star). Due to the planar nature of the evolution, matter - radiation coupling increases, and the color shell propagates outwards with time. Since the structure of the breakout shell is not well described by pure hydrodynamic models, NS10 roughly estimated it as a simple rarefaction wave (assumption 8 in section 2). In the numerical calculation, we found a different evolution of the breakout shell structure, which originates in the fact that the initial density profile is not constant. As a result, the color shell propagates outwards faster than predicted, and the temperature drops more rapidly than predicted with $\beta_P = 0.45$. By the transition to the spherical phase, sideways expansion becomes important and the envelope becomes more transparent. Therefore, the coupling decreases and the color shell propagates inwards. Nevertheless, the color shell is still outer than the breakout shell. NS10 neglected this phase, as they assumed that when the spherical phase begins, the color shell propagates very rapidly to a point inner to the breakout shell. We find here that this phase cannot be neglected and that during this phase $\beta_{S,1} = 0.35$. Only when the thermalization point reaches the breakout shell, a third phase begins. At this phase, the temperature drops with $\beta_{S,2} = 0.6$ as predicted by NS10 for the spherical phase, because the hydrodynamic evolution at locations inner than the breakout shell is well described by their model.

In addition to the different temporal behavior, the typical parameters of the observed temperature should be calibrated. We first find that η_0 is better estimated as

$$\eta_0 \approx 0.8 \left(\frac{v_0}{10^4 \text{ km/s}} \right)^{\frac{15}{4}} \left(\frac{\rho_0}{10^{-9} \text{ g/cm}^3} \right)^{-\frac{1}{8}}. \quad (9)$$

This scaling is similar to equation 10 in NS10, only with a higher numerical factor⁴. It is obtained by examining several calculations with $T_{\text{BB},0} \approx T_{\text{obs}}$, and demanding $\eta_0 = 1$ for breakouts in which $T_{\text{BB},0} = T_{\text{obs}}$, i.e., the breakout shell is the color shell. Besides the different value of η_0 , the initial observed temperature, given in equation 8 scales as $\eta_0^{0.07}$ instead of $\eta_0^{0.14}$ as predicted. This is also due to the differences in the hydrodynamic structure of the breakout shell.

The diffusion time at the breakout and the planar to spherical transition time are the same as in the luminosity analysis, and are given in equations 6. A scaling relation for the third phase transition time can be obtained by observing equation 18 at NS10 and noting that for the breakout shell

$$\eta(m_0, t) = \eta_0 \left(\frac{t_s}{t_0} \right)^{-1/6} \left(\frac{t}{t_s} \right)^{\frac{42n+49}{12(1.19n+1)}}. \quad (10)$$

Since the breakout shell is also the color shell when $\eta = 1$,

⁴ The lower coupling, reflected by the higher numerical factor, is a net result of the inclusion of bound-free transitions to the opacity, which increases the coupling by a factor of 4 at breakout temperatures, and the higher breakout shell temperature (see equation 4) and shorter diffusion time (see equation 6a) both decrease the coupling.

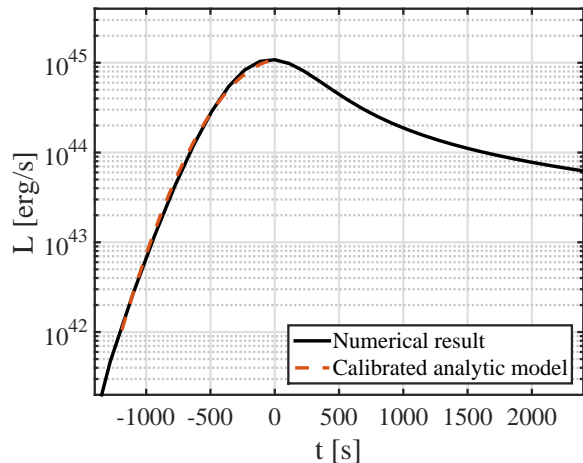


Figure 5. The bolometric luminosity of a typical analytic RSG progenitor during the breakout pulse. The numerical result (solid black line) is compared to the calibrated analytic model (dashed red line), described in equation 13. The progenitor and explosion properties are $M_{\text{ej}} = 15M_{\odot}$, $R_{*} = 500R_{\odot}$ and $E_{\text{exp}} = 10^{51} \text{ erg}$.

we deduce the transition time is

$$t_c = 6.5t_s \left(\frac{1}{\eta_0} \right)^{\frac{12(1.19n+1)}{42n+49}} \left(\frac{t_s}{t_0} \right)^{\frac{2(1.19n+1)}{(42n+49)}}. \quad (11)$$

For RSG progenitors ($n = 1.5$) we obtain

$$t_c = 6.5t_s \eta_0^{-0.3} \left(\frac{t_s}{t_0} \right)^{0.05}. \quad (12)$$

The numerical calibration factor of 6.5 is chosen to best fit the numerical simulations. This model fits the numerical temperature well, as demonstrated in figure 3.

3.3 The breakout pulse

During the breakout, the typical timescale is t_0 , which is also the diffusion time at breakout (equation 6). At early stages of the rise (before breakout), emission is due to photons diffusing ahead of the shock when the shock is far from the edge. The fraction of photons that diffuse a length x ahead of the shock is e^{-x^2} , and since the shock distance from the edge at each time is approximately $x = -v_0 t$ (t is negative), the early rise should be dominated by a e^{-t^2} term. Around the breakout (i.e. $\tau \simeq c/v$), however, the energy scales as e^{-x} (Weaver 1976). We therefore follow a method similar to the one discussed in Sapir et al. (2011), and approximate the light curve during the rise ($t < 0$) as

$$L(t) = L_0 e^{-a(t/t_0)^2 - b(t/t_0)}, \quad (13)$$

where L_0, t_0 are defined in equation 6. The best fit to the rise is obtained for $a = 0.35$, $b = -0.15$ and is shown in figure 5.

The observed temperature during the breakout changes by less than 5% from the time in which $L(t) = 0.1L_{\text{peak}}$ to the peak time, and therefore it can be approximated as a constant.

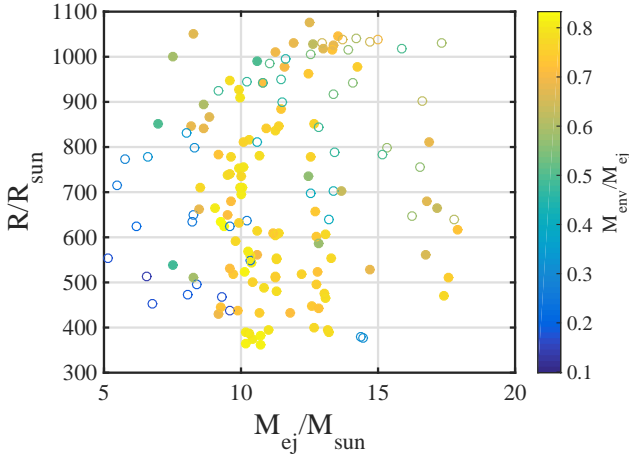


Figure 6. The properties of the stars that were numerically calculated using MESA, and classified as realistic type II-P/II-L progenitors. The different colors represent different values of the ratio $M_{\text{env}}/M_{\text{ej}}$, where M_{env} is the envelope mass and M_{ej} is the ejecta mass. The filled circles represent progenitors with $M_{\text{ZAMS}} \leq 20M_{\odot}$ which are more common.

4 NUMERICAL LIGHT CURVES OF NUMERICAL PROGENITORS

In this section we study the light curves generated by explosions of more realistic progenitors, whose structure is calculated numerically using a stellar evolution code. Since the progenitor structure depends on various initial parameters such as mass, rotation and metallicity, and on unknown fudge factors used by the code, such as a mixing length coefficient, we have calculated a large set of progenitors and calculated the light curves that they generate upon explosion. The numerical progenitors have unique profiles, and specifically their density near the edge is not well characterized by a single power law with index n .

The stellar evolution of the progenitor models was followed using the publicly available package MESA version 6596 (Paxton et al. 2011, 2013, 2015). To produce a wide range of progenitors, we varied the zero age main sequence (ZAMS) mass between $[10, 50]M_{\odot}$, the metallicity between $[2 \times 10^{-5}, 2 \times 10^{-2}]$, the mixing length parameter between $[1.5, 5]$, and the initial rotation rate between $[0, 0.8]$ of the breakup rotation rate. In all models, mass loss was determined according to the “Dutch” recipe in MESA, combining the rates from Glebbeek et al. (2009); Nieuwenhuijzen & de Jager (1990); Nugis & Lamers (2000); Vink et al. (2001), with a coefficient $\eta = 1$, the convection was according to the Ledoux criterion, with a semi-convection efficiency parameter $\alpha_{sc} = 0.1$ (Paxton et al. 2013, eq. 12), and exponential overshoot with parameter $f = 0.008$ (Paxton et al. 2011, eq. 2).

A total of 219 progenitors were calculated. Out of them, we chose 124 who are more realistic type II-P/II-L SN candidates, by choosing progenitors with $M_{\text{env}} \geq 4M_{\odot}$ and $R_* \geq 100R_{\odot}$. The stars that were cut do not have large enough radii and mass to emit detectable cooling envelope radiation for several weeks. In order to simulate the explosion, we cut out the ^{28}Si core, and referred to everything outside that core as ejecta. Then, we planted the explo-

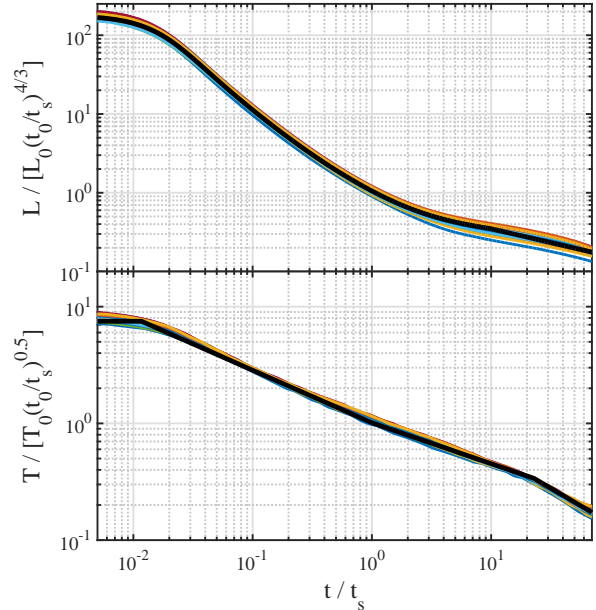


Figure 7. Bolometric luminosity and observed temperature obtained numerically for 20 numerical RSG progenitors from our sample (light travel time ignored). The time for each light curve is normalized by t_s as obtained by the calibrated analytic model. L and T are normalized by their value at t_s , as predicted by the analytic model. Also shown is a normalized light curve of the calibrated analytic model (black thick line). This figure shows that all progenitors produce rather similar light curve shapes, with a smaller spread before t_s than after t_s . It also illustrates that the calibrated analytic model provides a good fit to the numerical one.

sion energy as thermal energy in the 5 innermost cells of the ejecta. The properties of the different progenitors are specified in figure 6, where the envelope begins at boundary between the helium shell and the hydrogen shell, where a sharp density drop exists. Full data is given in appendix C.

4.1 Bolometric light curve and observed temperature as functions of the breakout properties

In figure 7, typical normalized light curves from 20 different progenitors are presented. The time axis is normalized to the model spherical time (equation 6b), and the bolometric luminosity and observed temperature are normalized to the values given by the model at $t = t_s$, (equations 5, 8 respectively). Namely, the normalization is done based on the parameters of the breakout shell. Figure 7 also shows our analytic model (equations 5-9 and 12), normalized similar to the numerical light curves (black thick line). The figure shows that all the light curves are similar, and that the calibrated analytic model (which relates breakout parameters to the light curve) fits the numerically calculated progenitors as well as the analytic ones. In fact, the relations between the luminosity and temperature evolution and the properties of the breakout shell, that were specified in equations 5-9 and 12, fit the emission of the numerical progenitors without further adjustments. It fits the luminosity to within

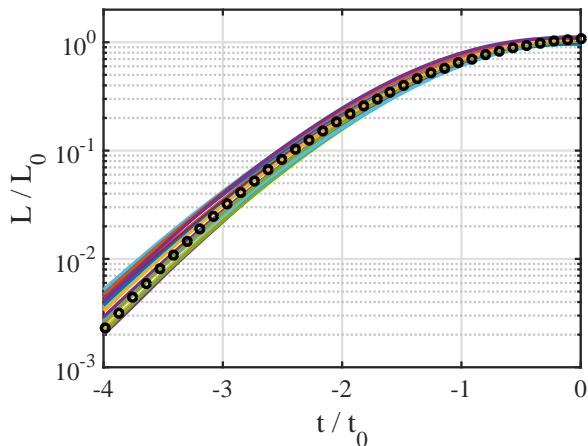


Figure 8. Bolometric light curves during the breakout pulse, of 20 numerical RSG progenitors. The luminosity is normalized to L_0 and the time is normalized to t_0 (equation 6a). The analytic model for the rise, given in equation 13 is marked in black circles.

15% and the temperature to within 10% until well within the spherical phase. At $t \gtrsim 4t_s$ there is a slightly larger spread in the luminosity evolution of different progenitors, since the spherical phase luminosity power-law index α_s , is somewhat dependent on the inner progenitor structure, and because larger progenitors yield a more rapid luminosity decrease (as described in section 3). The luminosity fit is then accurate to within 30%.

The similar light curve evolution of different progenitors during the planar phase is expected and it is a result of the light curve being mostly determined at the breakout shell. The spherical phase however probes inner layers of the progenitor and therefore the observed similarity is less obvious. The similar emission of different progenitors during the spherical phase implies that the early light curve depends weakly on the density profile, as suggested by the weak dependence on n in analytic progenitors. We therefore expect the model based on the breakout properties to be applicable for a wide range of structures including such that are significantly different than those in our sample.

The breakout pulse is also well approximated by the analytic model specified in equation 13. The numerical light curves and analytic model are shown in figure 8. During the last decade of rise, the analytic model fits the numerical results better than 30%, while earlier it fits to a factor of 2.

4.2 The observed spectrum

Earlier analytic works, as well as some numerical studies, assumed the observed spectrum was a blackbody with temperature T_{obs} (approximation 4 in section 2). However, this is not exactly true. At high frequencies ($h\nu > 3k_B T$, where k_B is Boltzmann constant and h is Planck constant) the emission is suppressed due to line blanketing, while at low frequencies ($< k_B T$), namely the Rayleigh-Jeans regime, a deviation is expected even when line emission and absorption is neglected. Deviations from blackbody spectrum at the Rayleigh-Jeans regime are especially important during very early times (breakout and planar phase), when the tem-

perature is $\approx 10^5$ °K and most of the radiation is emitted at frequencies higher than the optical/UV bands. During these times, even a small deviation from a pure blackbody can significantly affect the observed light curve. As we explain below, such deviation is expected, and also seen in simulation results where radiation transfer is solved more accurately than our code (e.g., Tominaga et al. 2011). Below we derive an analytic approximation to the observed spectrum in the Rayleigh-Jeans regime and compare it to the results of Tominaga et al. (2011).

The color shell (a.k.a. thermalization depth) is the outermost point where a significant number of photons with $h\nu \sim k_B T_e$ is created (hence $\eta = 1$). Here, T_e is the local electron temperature. It is also the outermost point where such photons are absorbed (hence $\tau_{\text{abs}}\tau = 1/3$). Outer to this point, the energy flux is dominated by these photons and therefore the color temperature of the radiation is constant (and equals T_{obs}). However, at lower frequencies the spectrum continues to change, since photon opacity is frequency dependent, and so is the absorption optical depth to the observer, denoted here as $\tau_{\nu,\text{abs}}$ (not to be confused with τ_{abs} , which is the Planck mean optical depth). When free-free and bound-free processes dominate the absorption, $\tau_{\nu,\text{abs}}$ is larger for lower frequency photons. As a result, the number of photons with $h\nu < k_B T_{\text{obs}}$ is set outer to the color shell, at the point where $\tau_{\nu,\text{abs}}\tau \approx 1/3$ and the electron temperature, T_e , is lower than T_{obs} . We use this criterion and post process the observed spectrum from our numerical hydrodynamic profiles. An example of such spectrum is depicted in figure 9.⁵

In order to obtain an analytic approximation for the spectrum, we approximate the density profile during the expansion as a power-law,

$$\rho(\tau) \propto \tau^k. \quad (14)$$

In most of our progenitors, $k \approx 1$ around the breakout and later (the analytic solution yields $k = 11/12$ during the spherical phase). Outer to the luminosity shell, the luminosity is constant and it is $L \propto r^2 U_r / \tau$ where U_r is the radiation energy density. During the breakout and the planar phase r is roughly constant, and during the spherical phase the sharp density gradient dictates that r varies slowly with τ . Therefore we can approximate $U_r \propto \tau$. By assuming $U_r = a_{BB} T_e^4$ we obtain

$$T_e(\tau) = T_{\text{obs}} \left(\frac{\tau}{\tau_{\text{obs}}} \right)^{1/4}, \quad (15)$$

where $\tau_{\text{obs}} [\tau_{\text{abs,obs}}]$ is the diffusion [absorption] optical depth where $T = T_{\text{obs}}$. The absorption opacity (bound-free and free-free) is approximately proportional to

$$\kappa_{\nu,\text{abs}}(r) \propto \rho T_e^{-0.5} \nu^{-3} (1 - e^{-h\nu/k_B T_e}). \quad (16)$$

Substituting equations 14 - 15 into equation 16 we obtain

⁵ We note that although our code does allow for different photon and electron temperatures, the calculation of T_e in regions where the radiation spectrum is not a blackbody is not fully accurate as the heating term in equation A2a implicitly assumes a blackbody spectrum. Nevertheless, since the drop in electron temperature at lower optical depth depends mostly on the drop in the radiation energy density, which is accounted for in the code, it does provide a reasonable approximation of T_e .

the following expression for the absorption opacity at the Rayleigh-Jeans regime ($h\nu \ll k_B T_{\text{obs}}$):

$$\tau_{\nu, \text{abs}}(r) = \tau_{\text{abs, obs}} \left(\frac{h\nu}{3k_B T_{\text{obs}}} \right)^{-2} \left(\frac{\tau}{\tau_{\text{obs}}} \right)^{\frac{15k+8}{8(k-1)}}. \quad (17)$$

We define $\tau_{\text{col}}(\nu)$ as the optical depth at the point where $\tau_{\nu, \text{abs}} \tau_{\text{col}}(\nu) = 1/3$. Equation 17 dictates then

$$\tau_{\text{col}}(\nu) = \tau_{\text{obs}} \left(\frac{h\nu}{3k_B T_{\text{obs}}} \right)^{\frac{16k}{13k+8}}. \quad (18)$$

Since $k \approx 1$ in most cases, the power of ν is approximately $16/21$. Substituting equation 18 into equation 15 we find that the electron temperature observed at each frequency is

$$T_{\text{col}}(\nu) \approx T_{\text{obs}} \left(\frac{h\nu}{3k_B T_{\text{obs}}} \right)^{0.2}; \quad h\nu < k_B T_{\text{obs}} \quad (19)$$

for the Rayleigh-Jeans regime. Since the luminosity is constant outer to the luminosity shell, the frequency dependence of T_{col} implies that the modified Rayleigh-Jeans spectrum is $L_\nu \propto \nu^{1.4}$. At high frequencies ($h\nu > 3k_B T_{\text{obs}}$) we assume that the thermalization depth is τ_{obs} , meaning $T_{\text{col}}(\nu) = T_{\text{obs}}$. By comparing the analytic model to numerical results we find that the spectrum, including the peak, is best fit as a harmonic sum

$$T_{\text{col}}(\nu) = T_{\text{obs}} \left(1 + \left(\frac{h\nu}{3k_B T_{\text{obs}}} \right)^{-0.2 \cdot m} \right)^{-1/m} \quad (20)$$

with $m > 10$ (sharp transition at $h\nu = 3k_B T_{\text{obs}}$). The luminosity at each wavelength is then given by

$$L_\nu = 0.9L \cdot \frac{15}{\pi^4} \left(\frac{h}{k_B T_{\text{col}}(\nu)} \right)^4 \nu^3 \cdot \left(e^{\left(\frac{h\nu}{k_B T_{\text{col}}(\nu)} \right)} - 1 \right)^{-1}, \quad (21)$$

The factor of 0.9 is obtained by demanding the integral of the spectrum over ν to equal to L . Figure 9 depicts a comparison between equation 21 and a spectrum calculated numerically by post-processing the hydrodynamic profiles obtained short time after a breakout (in this case $T_{\text{obs}} = 3.8 \cdot 10^5$ °K and $L = 1.6 \cdot 10^{45}$ erg/s). Generally, we find that for the optical and UV bands the analytic model deviates by less than 25% from the numerical results at all times.

While deriving equation 21 we assumed that $T_{\text{col}}(\nu)$ is set in a diffusion optically thick region, namely $\tau_{\text{col}}(\nu) > 1$. Therefore, equation 18 implies that equation 21 is valid only for frequencies higher than a critical frequency which satisfies $h\nu \approx \tau_{\text{obs}}^{-1.3} (3k_B T_{\text{obs}})$. Below this frequency the spectrum is better described by a blackbody (i.e., $L_\nu \propto \nu^2$). For the progenitors and explosion energies we explored this critical frequency is typically around the optical bands.

An additional condition that must be satisfied for our analytic approximation to be valid is that the luminosity shell is *deeply* within thermal equilibrium, i.e., $\eta(\tau = c/v) \ll 1$. The reason is that when $\eta(\tau = c/v) \approx 1$ the luminosity shell is also the color shell and the electrons in this shell have just enough time to cool down (by emitting photons) so $U_r = aT_e^4$. Therefore, outer shells (with $\tau < c/v$) do not have enough time to cool down and our approximation of $U_r = aT_e^4$ is not valid. In fact when $\eta(\tau = c/v) \sim 1$ a blackbody is probably a better approximation for the observed spectrum.

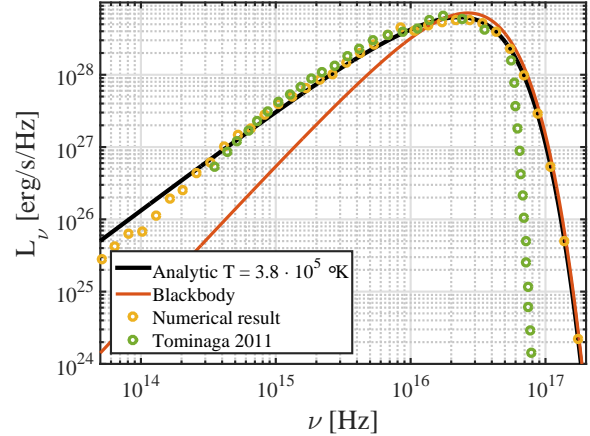


Figure 9. The spectrum emitted from the same progenitor as in figure 10 at $t \approx 300$ s after the breakout, when $T_{\text{obs}} = 3.8 \cdot 10^5$ °K. The analytic model (solid blue line) fits both our numerical result (yellow circles) and the result of Tominaga et al. (2011) (green circles, see text) to within 20% at frequencies below the spectral peak. At frequencies much above the peak the spectrum of Tominaga et al. (2011) falls faster as they account for line blanketing while we do not. A blackbody spectrum at the same temperature is depicted for comparison (solid red line).

This condition, $\eta(\tau = c/v) \ll 1$, is typically satisfied for RSG explosion as discussed in section 4.5.

In order to test our analytic (and numerical) spectra we compare our results to a spectrum presented in Tominaga et al. (2011). They find the spectrum using the numerical code STELLA (Blinnikov et al. 1998), which uses a multi-group radiative transfer and does not need to employ many of the approximations we use here in order to derive the observed spectrum. Figure 9 depicts, in addition to our analytic and numerical spectra, a spectrum taken from figure 2a ($t = 0$) in Tominaga et al. (2011). They calculated this spectrum at the breakout of an explosion with $E_{\text{exp}} = 10^{51}$ erg, $R_* = 795R_\odot$ and $M_{\text{ej}} = 16.8M_\odot$. Our spectra are taken from an explosion with $E_{\text{exp}} = 10^{51}$ erg, $R_* = 624R_\odot$ and $M_{\text{ej}} = 9.3M_\odot$. Therefore L and T_{obs} are expected to be slightly different. In figure 9 we multiply their luminosity by a factor of 1.5 and divide our breakout temperature by 1.15, so the peak of their spectrum coincides with ours. The comparison shows a very good agreement of the spectral shape in the Rayleigh-Jeans regime and near the peak of L_ν . Above the peak, their spectrum falls faster than ours since their code includes line blanketing while we neglect it.

4.3 The effect of light travel time

The model described in sub-sections 3.2 & 4.1 neglects light travel time, though it must be considered at times where $t \lesssim R_*/c$. Radiation emitted at small angles relative to the line which connects the source to the observer, travels a shorter distance to the observer and is thus detected earlier than radiation emitted at large angles. This yields a smearing of each point in the source frame light curve as a rectangular pulse of width $t_{\text{RC}} = R_*/c$ and height $L(t)/t_{\text{RC}}$ where $L(t)$ is

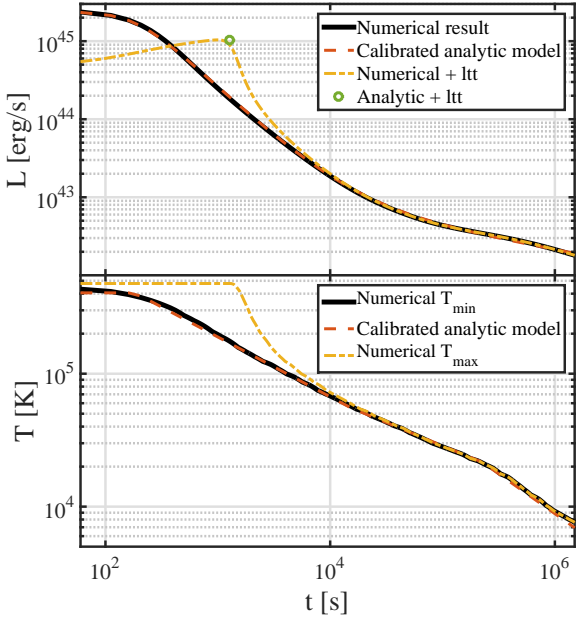


Figure 10. Top: the bolometric luminosity of a typical numerical RSG progenitor after the peak. Shown are the numerical result (solid black line) and the analytic model (dashed red line) where light travel time effects are neglected, and the same numerical result, with light travel time effects included (dotted-dashed yellow line). The analytic estimation to the peak with light travel time (equation 24) is marked by a green circle. Bottom: the observed temperature of the same progenitor after the peak. Light travel time causes the observer to see a range of temperatures. T_{\min} (solid black line) is the line-of-sight temperature (i.e., the same as in the model where light travel time is ignored), while T_{\max} (solid yellow line) is calculated using equation 26. The analytic model without light travel time is plotted in dashed red line. The progenitor and explosion properties are $M_{\text{ej}} = 9.3M_{\odot}$, $R_* = 624R_{\odot}$ and $E_{\text{exp}} = 10^{51}\text{erg}$. For this progenitor, $t_0 = 180\text{s}$ and $t_{\text{RC}} = 1450\text{s}$.

the luminosity in the source frame (Katz et al. 2012). The luminosity observed at each time due to this effect is

$$L_{\text{ltt}}(t) = \frac{1}{t_{\text{RC}}} \int_{t-t_{\text{RC}}}^t L(t') dt'. \quad (22)$$

For most RSG progenitors $t_{\text{RC}} \ll t_s$, as demonstrated in section 5. Therefore, light travel time is important only during the breakout pulse and early in the planar phase. The exact observed luminosity can be obtained from the model of the source frame luminosity by accounting for the effect numerically (using equation 22). For the convenience of the reader, we present a simple analytic estimate of the peak bolometric luminosity, including light travel time, and the time of the peak when light travel time is considered, relative to the peak when it is not.

Since the rise is much faster than the fall, only emission from the last t_0 before the peak contributes to the peak luminosity, and the peak time is approximately $t_{\text{peak,ltt}} = t_{\text{RC}} - t_0$, where again $t = 0$ is defined as the peak of bolometric emission without light travel time. The peak luminosity,

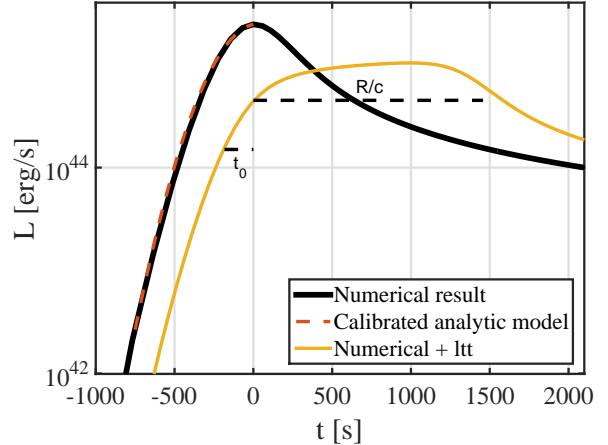


Figure 11. The bolometric luminosity of the same progenitor from figure 10 during the breakout pulse. Both the numerical result (solid black line) and the analytic model (dashed red line) neglect light travel time. The same numerical result, after accounting for light travel time (solid yellow line) is composed of an exponential rise at early times, a slower rise from $t = 0$ to $t = t_{\text{RC}}$ and a rapid decline thereafter.

light travel time included, is then given by

$$L_{0,\text{ltt}} = L_0 \frac{t_0}{t_{\text{RC}}} + \frac{1}{t_{\text{RC}}} \int_{t=0}^{t_{\text{RC}}-t_0} L(t') dt', \quad (23)$$

where $L(t')$ is given by equation 5. Integration (during the planar phase) yields

$$L_{0,\text{ltt}} = L_0 \frac{3t_0}{t_{\text{RC}}} f, \quad (24)$$

where f is a numerical factor which equals

$$f = \frac{5}{3} - \left(\frac{t_{\text{RC}}}{t_0} - 1 \right)^{-1/3}. \quad (25)$$

The value of f varies between 0.8 and 1.2 for most progenitors. Figure 10 shows the calculated emission for a typical numerical progenitor, after the peak, with and without light travel time (in log-log scale). In addition are shown the analytic model (without light travel time) and the analytic estimate for the peak luminosity and peak time including light travel time. The calculated light curve before and after the peak is shown in figure 11 (in semi-log scale). During the early rise, the shape of the pulse is weakly affected by light travel time because of the rapid increase. Therefore, the smeared emission rises during a typical timescale t_0 . Then, it rises slowly (changes by less than a factor of 2) from $t = 0$ to $t_{\text{peak,ltt}}$, reaches the estimated peak value $L_{0,\text{ltt}}$ and falls faster than the planar power law during a typical timescale t_0 until it coincides with the source frame light curve.

Due to light travel time, the spectrum also changes. As the source frame temperature drops with time, low frequency photons arrive at the observer from small angles with respect to the line of sight at the same time that high frequency photons arrive from large angles. During the breakout and the exponential rise, only small angles contribute to the emission, so the spectrum is similar to the breakout spectrum at the source frame. From around the peak at the source frame, the spectrum is composed of three different regions:

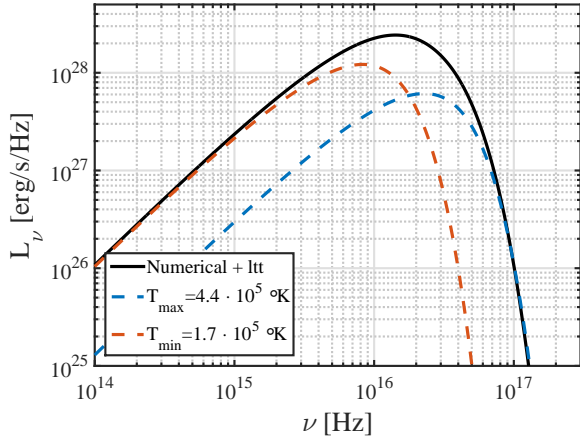


Figure 12. The spectrum emitted from the same progenitor as in figure 10, at $t = t_{\text{RC}}$. The observed spectrum (solid black line) accounts for light travel time and is therefore non-thermal. The relative contribution of T_{max} (dashed red line) and T_{min} (dashed orange line) is also shown.

A modified Rayleigh-Jeans ($\nu^{1.4}$) radiance with the temperature at angle $\theta = 0$, which we denote T_{min} , a relatively constant radiance to the temperature at the largest angle that contributes to the emission T_{max} , and an exponential fall. The calculated spectrum at $t = t_{\text{RC}}$ is shown in figure 12, and compared with the relative contribution of T_{min} and T_{max} .

The bottom of figure 10 depicts the observed temperature without light travel time, which is also T_{min} when light travel time is considered, the analytic model, and T_{max} , which is defined as⁶

$$T_{\text{max}} = T_{\text{obs}}(\max(t - t_{\text{RC}}, 0)). \quad (26)$$

4.4 The breakout shell parameters as a function of the progenitor properties

The analytic model that describes the emission as a function of the breakout shell properties, fits the results from analytic progenitors and from numerical progenitors, as described in sub-section 4.1. In this sub-section we relate the breakout parameters to the three global parameters M_{ej} , R_* and E_{exp} for our set of progenitors. This will enable us later to find the light curve dependence on these parameters.

The definition of the breakout time that we use in order to determine the breakout parameters is the same as described in section 3. At the breakout, $\tau_0 = 1.2c/v_0$ was obtained for the numerical stars, similarly to the analytic progenitors. The scaling of the breakout parameters for the numerical progenitors is similar to the analytic progenitors

⁶ At times earlier than $t_{\text{RC}} - t_0$, T_{max} is not determined at $\theta = 90^\circ$, since the emission at this angle is negligible compared to the emission from angles where light from the breakout has already reached the observer.

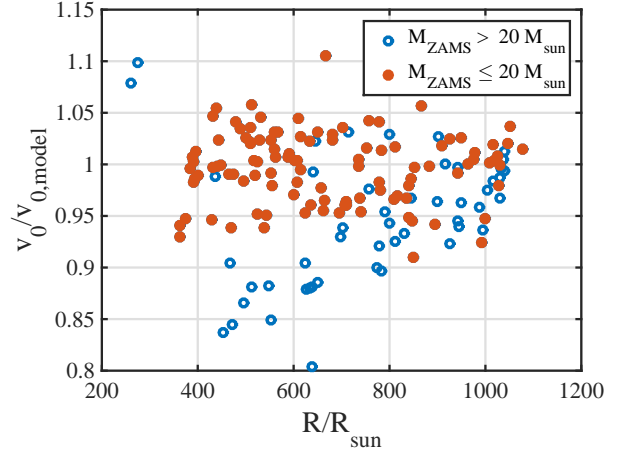


Figure 13. The values of v_0 , obtained numerically for all the numerical progenitors, normalized to the scaling of equation 27b. Progenitors with $M_{\text{ZAMS}} \leq 20$, which are more common, are marked with filled red circles, and the rest of the progenitors are marked with empty blue circles.

as well, except for the numerical coefficients and the R_* dependency:

$$\rho_0 \approx 1.5 \cdot 10^{-9} \text{ g/cm}^3 M_{15}^{0.67} R_{500}^{-0.64} E_{51}^{-0.31}, \quad (27a)$$

$$v_0 \approx 4500 \text{ km/s} M_{15}^{-0.44} R_{500}^{-0.49} E_{51}^{0.56}, \quad (27b)$$

$$\frac{d_0}{R_*} \approx 10^{-2} M_{15}^{-0.21} R_{500}^{-0.1} E_{51}^{-0.25}. \quad (27c)$$

Since R_* and M_{ej} are uncorrelated (see figure 6), the different R_* dependence is explicit. In figure 13 the ratio between the numerical values of v_0 and the prediction of equation 27b is depicted for all the progenitors, as a function of the progenitor radius. As can be seen, for all progenitors with $M_{\text{ZAMS}} \leq 20M_\odot$ the scaling is good to within 10% while for larger M_{ZAMS} progenitors it is accurate to within 20%.

Similar ratios for the breakout shell density and width are shown in figure 14 and figure 15 respectively. The scaling is good to within 20%. The scaling of all the breakout properties with the explosion energy was checked using simulations of the same progenitor in different energies, and was found to be within 1% (the expected numerical error).

The difference between the analytic model, specified in equations 2 and the numerical model of equations 27, mainly in R_* dependency, is due to the different stellar structure of progenitors with different radii. None of the progenitor's density profiles is exactly of a power law form, but, defining the density logarithmic index of the breakout shell,

$$n' \equiv \left. \frac{d \log(\rho)}{d \log(R_* - r)} \right|_{m=m_0}, \quad (28)$$

we find out that smaller progenitors tend to have higher values of n' . The value of n' changes from around 1.8 for progenitors with $R_* = 400R_\odot$ to around 0.8 for progenitors with $R_* = 900R_\odot$. In addition, the logarithmic index around

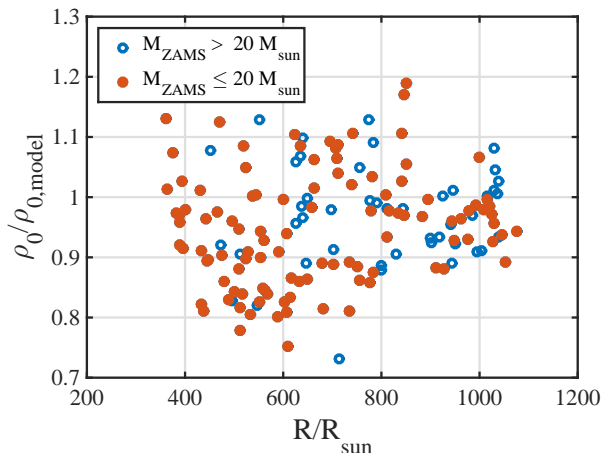


Figure 14. The values of ρ_0 , obtained numerically for all the numerical progenitors, normalized to the scaling of equation 27a. Symbols are the same as in figure 13.

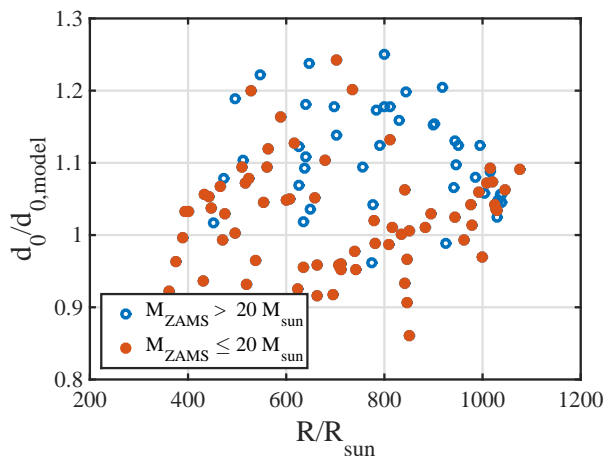


Figure 15. The values of d_0 , obtained numerically for all the numerical progenitors, normalized to the scaling of equation 27c. Symbols are the same as in figure 13.

the breakout shell generally varies less for smaller progenitors. An example for these phenomena is given in figure 16, in which two profiles of different progenitors, with similar masses and different radii are shown. This correlation between the progenitor radius and the mean and variance values of n affects the scaling of the breakout properties with the progenitor radius.

Using equations 27, it can be seen that equation 3 is not applicable for the numerical progenitors. Although $\tau_0 = 1.2c/v_0$, the relation $\tau \sim \kappa_T \rho_0 d_0$ is correct only to a (R_* dependent) factor of order of unity since n' and the structure vary. The equivalent of equation 3 for our numerical progenitors set is

$$d_0 = \frac{2.75c}{\kappa_T \rho_0 v_0 R_{500}^{0.23}}. \quad (29)$$

The dependence of the breakout shell temperature on

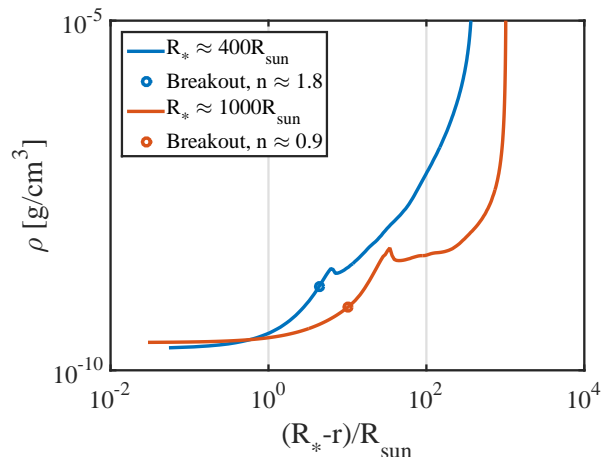


Figure 16. The density profiles of two numerical progenitors with a similar mass $M_{ej} = 12.5M_{\odot}$, as a function of the distance from the edge. The larger progenitor ($R_* \approx 1000R_{\odot}$) is characterized by $n' = 0.9$ and the smaller one ($R_* \approx 400R_{\odot}$) is characterized by $n' = 1.8$. In addition, the logarithmic index around the breakout shell varies less for the smaller progenitor, so it is better approximated as a power law density profile.

v_0 and ρ_0 is the same as in equation 4 (within 3% accuracy). Therefore, it is given by

$$T_{BB,0} \approx 5.4 \cdot 10^5 \text{ } ^\circ\text{K} M_{15}^{-0.05} R_{500}^{-0.4} E_{51}^{0.2}. \quad (30)$$

The scatter of the breakout shell temperature with respect to the model is determined by the scatter of $\rho_0^{0.25} v_0^{0.5}$, and is less than 10%.

4.5 Condition for breakout in thermal equilibrium

In our model for the observed temperature we assume that radiation is in thermal equilibrium. This is true at the time of the breakout when $\eta_0 > 1$, meaning that enough photons are generated within the breakout shell to maintain thermal equilibrium. If $\eta_0 < 1$, the emission is out of thermal equilibrium until at least the spherical phase (for further discussion see NS10). We can use our scaling of η_0 to provide an upper limit for the explosion energy for which the breakout is thermal. We substitute the scaling of the breakout properties from equation 27 into equation 9 and obtain

$$\eta_0 = 4 \cdot 10^{-2} M_{15}^{-1.73} R_{500}^{-1.75} E_{51}^{2.14}. \quad (31)$$

The maximal explosion energy for which the emission is in thermal equilibrium is therefore

$$E_{51} = 4.5 M_{15}^{0.81} R_{500}^{0.82}. \quad (32)$$

As can be seen, for a typical RSG explosion, the emission is indeed in thermal equilibrium from the breakout on.

5 A CALIBRATED ANALYTIC MODEL OF THE BOLOMETRIC LUMINOSITY AND OBSERVED TEMPERATURE

In this section, we summarize the results of the previous sections and present a calibrated analytic model for the evo-

lution of the luminosity and observed temperature. First (sub-section 5.1) we provide a model that is based on the properties of the breakout shell, v_0 , ρ_0 and R_* . This model is accurate and general in the sense that it is only weakly dependent on the exact properties of the progenitor structure. Then (5.2) we provide a model of the light curve as a function of the global explosion properties, E_{exp} , M_{ej} and R_* . This model is slightly less accurate than the first one and it is also less general, as it depends on the correlations between properties in our set of numerical progenitors. Times are denoted t_{hr} , and t_{day} for units of seconds, hours and days respectively. The time of the bolometric emission peak when light travel time is not considered is defined as $t = 0$. Bolometric and monochromatic light curves, calculated using the calibrated model presented in this section can be downloaded at <http://www.astro.tau.ac.il/~tomersh/>.

5.1 Bolometric light curve and observed temperature as functions of the breakout properties

The three parameters which characterise the breakout shell are v_0 , ρ_0 and R_* , since d_0 is determined via equation 29. We denote $v_{0,x} = v_0/(x \cdot 10^3 \text{ km/s})$, $\rho_{0,x} = \rho_0/(10^x \text{ g/cc})$ and $R_x = R_*/xR_\odot$.

The luminosity after the peak, neglecting light travel time, is obtained by substituting equations 6, 29 into equation 5:

$$\frac{L_{\text{obs}}(t)}{1 \text{ erg/s}} \simeq \begin{cases} 1.6 \cdot 10^{45} v_{0,5}^3 \rho_{0,-9}^1 R_{500}^2 & t \ll t_0 \\ 3.2 \cdot 10^{43} v_{0,5}^{0.33} \rho_{0,-9}^{-0.33} R_{500}^{1.69} t_{\text{hr}}^{-4/3} & t_0 \ll t \ll t_s \\ 3.3 \cdot 10^{42} v_{0,5}^{1.31} \rho_{0,-9}^{-0.33} R_{500}^{0.71} t_{\text{day}}^{-0.35} & t_s \ll t < t_{\text{rec}} \end{cases} \quad (33)$$

where t_{rec} is the time in which the observed temperature reaches $T = 7500^\circ\text{K}$. At this point, recombination is no longer negligible, and the model described here is no longer valid. To obtain a smooth broken power law, the luminosity at the transitions between the phases is given by a sum, as described in equation 7. During the breakout pulse ($t < 0$), the luminosity is obtained by substituting equation 6 into equation 13:

$$\frac{L_{\text{obs}}(t)}{1 \text{ erg/s}} \simeq 1.6 \cdot 10^{45} v_{0,5}^3 \rho_{0,-9}^1 R_{500}^2 e^{-0.35(t/t_0)^2 + 0.15(t/t_0)}. \quad (34)$$

The observed temperature after the peak is obtained by substituting equations 6, 9 and 12 into equation 8:

$$\frac{T_{\text{obs}}(t)}{1^\circ\text{K}} \simeq \begin{cases} 4.2 \cdot 10^5 v_{0,5}^{0.76} \rho_{0,-9}^{0.24} & t < t_0 \\ 1.1 \cdot 10^5 v_{0,5}^{-0.13} \rho_{0,-9}^{-0.21} R_{500}^{-0.1} t_{\text{hr}}^{-0.45} & t_0 \leq t < t_s \\ 3.3 \cdot 10^4 v_{0,5}^{-0.03} \rho_{0,-9}^{-0.2} R_{500}^{-0.2} t_{\text{day}}^{-0.35} & t_s \leq t < t_c \\ 4.1 \cdot 10^4 v_{0,5}^{-0.55} \rho_{0,-9}^{-0.18} R_{500}^{0.06} t_{\text{day}}^{-0.6} & t_c \leq t < t_{\text{rec}} \end{cases} \quad (35)$$

Before the peak, the observed temperature is roughly

constant. The observed spectrum is not blackbody, since higher energy photons are emitted from inner shells with higher temperatures. The observed spectrum is well described by equations 19, 21 until the peak of the spectrum, where line blanketing becomes significant. The transition times, and recombination time are given by

$$t_0 = 190 \text{ s } v_{0,5}^{-2} \rho_{0,-9}^{-1} R_{500}^{-0.23}, \quad (36a)$$

$$t_s = 3.2 \text{ hr } v_{0,5}^{-1} R_{500}^1, \quad (36b)$$

$$t_c = 2.5 \text{ day } v_{0,5}^{-2.07} \rho_{0,-9}^{0.08} R_{500}^{1.06}, \quad (36c)$$

$$t_{\text{rec}} = 17 \text{ day } v_{0,5}^{-0.92} \rho_{0,-9}^{-0.31} R_{500}^{0.1}. \quad (36d)$$

This model describes the luminosity for all numerically calculated progenitors to within 15% (30% late in the spherical phase) and the observed temperature to within 10%. This inaccuracy is due to the different structure of the progenitors.

In order to include light travel time, one should convolve the results given in this section with equation 22. The peak luminosity including light travel time is obtained by substituting equations 29 and 6 into equation 24:

$$L_{0,ttt} = 8 \cdot 10^{44} \text{ erg } v_{0,5} R_{500}^{0.77} f. \quad (37)$$

f is a numerical factor of order 1, given by equation 25. With light travel time included, the duration of the rise is of order $t_{\text{Rc}} = R_*/c$, while the initial rapid exponential rise is still characterised by a time scale t_0 . In addition, around the peak, the spectrum is not thermal, but characterised by a range of temperatures. For further discussion, see sub-section 4.3. A useful ratio to assess the importance of light travel time is

$$t_0/t_{\text{Rc}} = 0.16 v_{0,5}^{-2} \rho_{0,-9}^{-1} R_{500}^{-1.23}. \quad (38)$$

Examination of equations 33-37 shows that many of the observables (i.e., characteristic time scales and the luminosity and temperature at different regimes) depend strongly on v_0 and R_* . Therefore early observations will tightly constrain both parameters. However, only the rise time of the breakout pulse t_0 , depends strongly on ρ_0 . Without observations of the breakout with a temporal resolution of a minute or so, it will be hard to tightly constrain ρ_0 .

5.2 Bolometric light curve and observed temperature as functions of global SN properties

The three parameters which we use to characterise the SN are R_* , M_{ej} and E_{exp} . For the numerically calculated progenitors, the dependency of the breakout properties on these parameters is specified in equation 27. We denote $M_x = M_{\text{ej}}/xM_\odot$, $R_x = R_*/xM_\odot$ and $E_x = E_{\text{exp}}/10^x \text{ erg}$.

The luminosity after the peak, neglecting light travel time, is obtained by substituting equations 27 into equation 33:

$$\frac{L_{\text{obs}}(t)}{\text{erg/s}} \simeq \begin{cases} 1.8 \cdot 10^{45} M_{15}^{-0.65} R_{500}^{-0.11} E_{51}^{1.37} & t \ll t_0 \\ 2.7 \cdot 10^{43} M_{15}^{-0.34} R_{500}^{1.74} E_{51}^{0.29} t_{\text{hr}}^{-4/3} & t_0 \ll t \ll t_s \\ 1.6 \cdot 10^{42} M_{15}^{-0.78} R_{500}^{0.28} E_{51}^{0.84} t_{\text{day}}^{-0.35} & t_s \ll t < t_{\text{rec}} \end{cases} \quad (39)$$

Again, at the transitions between the phases, the luminosity is given by equation 7. Similarly, the luminosity during the breakout pulse ($t < 0$) obeys

$$\frac{L_{\text{obs}}(t)}{\text{erg/s}} \simeq 1.8 \cdot 10^{45} M_{15}^{-0.65} R_{500}^{-0.11} E_{51}^{1.37} e^{-0.35(t/t_0)^2 + 0.15(t/t_0)}. \quad (40)$$

The observed temperature after the peak is

$$\frac{T_{\text{obs}}(t)}{1^\circ\text{K}} \simeq \begin{cases} 4.3 \cdot 10^5 M_{15}^{-0.17} R_{500}^{-0.52} E_{51}^{0.35} & t < t_0 \\ 1 \cdot 10^5 M_{15}^{-0.07} R_{500}^{0.1} E_{51}^{-0.01} t_{\text{hr}}^{-0.45} & t_0 \leq t < t_s \\ 3 \cdot 10^4 M_{15}^{-0.11} R_{500}^{-0.04} E_{51}^{0.04} t_{\text{day}}^{-0.35} & t_s \leq t < t_c \\ 4.1 \cdot 10^4 M_{15}^{0.13} R_{500}^{0.46} E_{51}^{-0.25} t_{\text{day}}^{-0.6} & t_c \leq t < t_{\text{rec}} \end{cases} \quad (41)$$

Before the peak, the observed temperature is roughly constant. The observed spectrum is well described by equations 19, 21 up to frequencies higher than the peak of the spectrum, where line blanketing becomes significant. The transition times, and recombination time are given by

$$t_0 = 155 \text{ s } M_{15}^{0.23} R_{500}^{1.39} E_{51}^{-0.81}, \quad (42a)$$

$$t_s = 3.6 \text{ hr } M_{15}^{0.44} R_{500}^{1.49} E_{51}^{-0.56}, \quad (42b)$$

$$t_c = 3.2 \text{ day } M_{15}^{0.97} R_{500}^{2.02} E_{51}^{-1.19}, \quad (42c)$$

$$t_{\text{rec}} = 16.6 \text{ day } M_{15}^{0.22} R_{500}^{0.76} E_{51}^{-0.43}. \quad (42d)$$

This model describes the luminosity for all numerical progenitors to within 25% during the first day and 35% at later times. The observed temperature is described to within 15%. The inaccuracy is larger than the inaccuracy of the breakout properties model, since the scaling of the breakout properties with the progenitor properties is only accurate to within 20%. This model is also less general since it depends on the specific structures of the progenitors we calculated.

The peak luminosity including light travel time is

$$L_{0,\text{ltt}} = 7.2 \cdot 10^{44} \text{ erg } M_{15}^{-0.42} R_{500}^{0.28} E_{51}^{0.56} f, \quad (43)$$

where f is a numerical factor of order 1, given by equation 25 (see discussion at section 4.3). The ratio between the diffusion time at breakout and the light travel time is

$$t_0/t_{\text{Rc}} = 0.15 M_{15}^{0.23} R_{500}^{0.39} E_{51}^{-0.81}. \quad (44)$$

In the previous subsection (5.1) we deduced that all the observables, except for t_0 , depend mostly on two parameters (v_0 and R_*). This is also the case here where the observables depend strongly on R_* and $E_{\text{exp}}/M_{\text{ej}}$ (which is tightly related to v_0) but weakly on E_{exp} and M_{ej} separately. The

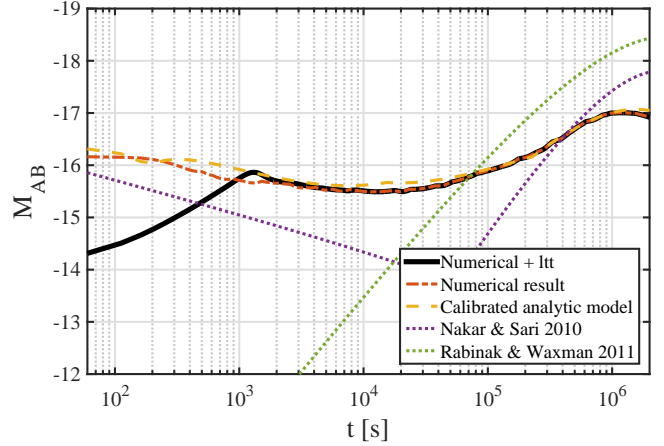


Figure 17. The R-band ($\lambda = 640\text{nm}$) light curve, for the same numerical progenitor as used in figure 10. The numerical result with (without) light travel time is plotted in a solid black (dotted-dashed red) line. It is compared to the analytic model (dashed orange line), which is obtained by substituting equations 39, 41 into equation 21. Also plotted are the models of NS10 (dotted purple line) and RW11 (dotted green line).

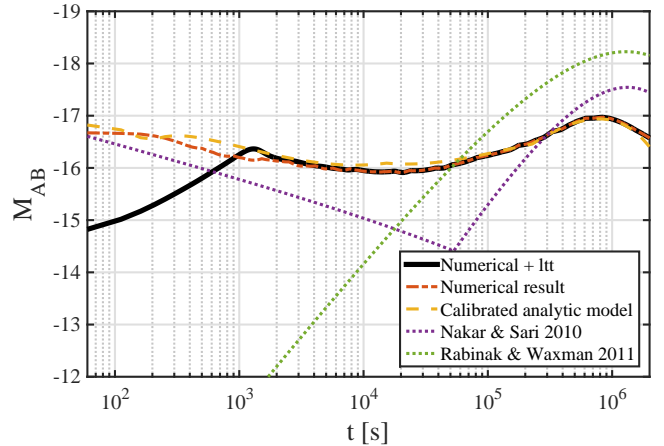


Figure 18. The g -band ($\lambda = 470\text{nm}$) light curve, for the same numerical progenitor as used in figure 10. Symbols are the same as in figure 17.

only exception, again, is t_0 . Therefore, detailed early light curve observations will provide tight constraints on R_* and $E_{\text{exp}}/M_{\text{ej}}$, but unless the rise of the breakout pulse, which is on a time scale of minutes, is resolved, it will be hard to constrain E_{exp} and M_{ej} separately.

6 PROPERTIES OF THE OPTICAL & UV LIGHT CURVE

In this section we discuss the properties of the optical & UV light curve at early times. A monochromatic light curve can be obtained for every wavelength, by substituting L, T from equations 39 - 41 into equation 21. Equation 21 is inaccurate for photon energies above those of the blackbody peak ($h\nu \gtrsim 3k_B T$) due to line blanketing. Therefore, the

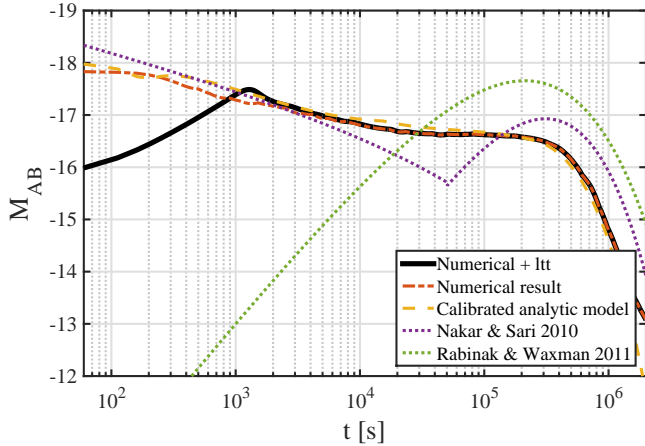


Figure 19. The near-UV ($\lambda = 200\text{nm}$) light curve, for the same numerical progenitor as used in figure 10. Symbols are the same as in figure 17.

monochromatic light curves presented here are inaccurate at times after the peak is seen in the specific observed wavelength, as line blanketing causes the decline after the peak to be faster than predicted by our model.

6.1 Emission after the breakout pulse

We give examples of the emission in R-, g -, and near-UV bands. Numerical light curves for R-band ($\lambda = 640\text{nm}$), with and without light travel time, are plotted in figure 17. The calculation was performed with the same progenitor as in figure 10, but the observed features are similar for all the progenitors in our sample. This result is compared to the optical emission obtained by substituting the model for L and T (section 5) into equation 21, and to the models of NS10 and RW11.

Our model fits the calculation (neglecting light travel time) within 0.2 mag. The emission is double peaked, as expected in NS10, although the first peak is less pronounced compared to their prediction. During the planar phase, the optical bands are in the modified Rayleigh-Jeans regime where⁷ $L_\nu \propto L/T^{2.4} \propto t^{-0.25}$. By the beginning of the spherical phase, the luminosity falls more slowly and the temperature falls faster, thus the monochromatic luminosity rises ($L/T^{2.4} \propto t^{0.5}$). After $t = t_c$ the rise is even more rapid ($L/T^{2.4} \propto t^1$), though by this time most of the wavelengths are not purely in the Rayleigh-Jeans regime. Light travel time affects the emission at times earlier than $t_{Rc} - t_0$, which is the peak time of the emission with light travel time included.

Similar light curves for the same progenitor are depicted in figure 18 at g -band ($\lambda = 470\text{nm}$) and in figure 19 at near-UV ($\lambda = 200\text{nm}$). The g -band light curves show features similar to that of the R-band. The main difference is that the rise is less rapid and the peak is seen a few days earlier

⁷ NS10 predicted $T \propto t^{-0.35}$ during the planar phase, while we find $T \propto t^{-0.45}$. However, NS10 assumed a blackbody spectrum which yields $L_\nu \propto L/T^3 \propto t^{-0.3}$ during the planar phase, so the decline is similar.

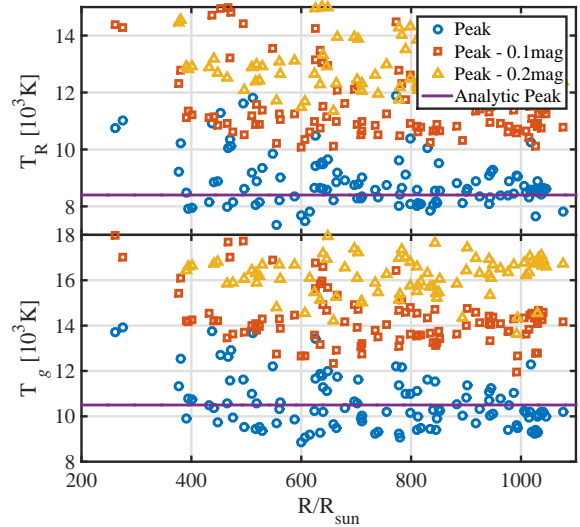


Figure 20. Top: the observed temperature at the peak of the R-band ($\lambda = 640\text{nm}$) as a function of the stellar radius (blue circles), calculated numerically for all the numerical progenitors. The temperature when the luminosity is lower by 0.1 mag (red rectangles) and by 0.2 mag (yellow triangles) is also shown. The purple line depicts the analytic prediction $x_{\text{peak}} = 2.7$. Bottom: the same for the g -band ($\lambda = 470\text{nm}$), where $x_{\text{peak}} = 2.9$

(see discussion below). For the near-UV, only one peak exists, followed by a slow decline that becomes after T_{obs} falls below the observed band a very fast decline. This feature is generic for most of the numerical progenitors. Since our model does not account for line blanketing, we expect a more rapid decrease than predicted by our blackbody model after the end of the slow decrease ($t \approx 5$ days) in the near-UV emission.

The second peak in the optical bands is seen when the observed band approaches the peak of the spectrum due to the decrease in the observed temperature. This happens at earlier times for bluer bands. By this time, the observed band is no longer in the Rayleigh-Jeans regime. The value of $x \equiv h\nu/k_B T_{\text{obs}}$ at the peak can be estimated based on equation 21 and depends on the evolution of T and L . For the late spherical phase $t \geq t_c$ our model predicts $x_{\text{peak}} = 2.95$. For both R- and g -band light curves, the peak is reached at times later than t_c . The peak time is obtained by substituting equation 41 into $T(t) = h\nu/k_B x_{\text{peak}}$:

$$\frac{t_{\text{peak}}}{1\text{day}} = 4.9 M_{15}^{0.22} R_{500}^{0.76} E_{51}^{-0.43} \nu_{15}^{-1.67} \left(\frac{x_{\text{peak}}}{2.95} \right)^{1.67}. \quad (45)$$

The R_* dependence of t_{peak} is similar to the result of Morozova et al. (2016) (equation 4) which found $t_{\text{peak}} \propto R_*^{0.82}$. Figure 20 depicts the temperature at the peak of R- (top) and g - (bottom) bands, and at 0.1 mag and 0.2 mag fainter than the peak, for all the progenitors. For the g -band, the peak temperature is around $T = 10000\text{K}$, which corresponds to $x_{\text{peak}} = 2.9$, while for the R-band the peak temperature corresponds to $x_{\text{peak}} = 2.7$. The slightly lower values of x_{peak} , compared to the model, are due to the steeper luminosity decrease near the time of recombination (figure 7). Note that the temperature is significantly higher than at the peak, by about 25% [40%], when the optical luminosity

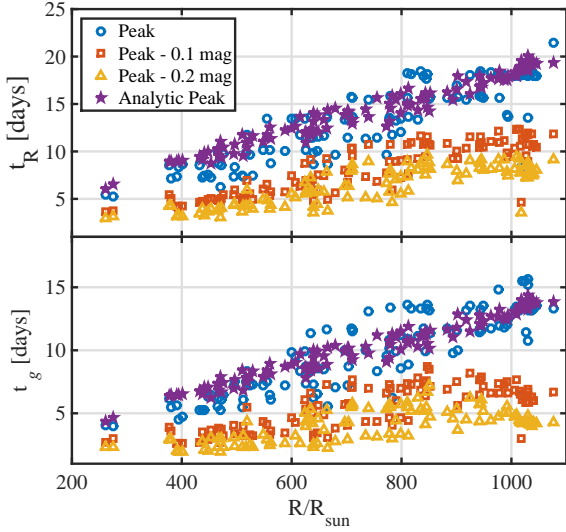


Figure 21. Top: the peak time (blue circles), and the times where the luminosity is lower by 0.1 mag (red squares) and 0.2 mag (yellow triangles), for the R-band ($\lambda = 640\text{nm}$) light curve as a function of the stellar radius. The times are calculated numerically for all the numerical progenitors. The analytic prediction (see equation 45) is marked by purple pentagrams. Bottom: the same for the g -band ($\lambda = 470\text{nm}$)

is only 0.1 [0.2] mag fainter. In figure 21 the peak time and the times where the luminosity is lower by 0.1 mag and 0.2 mag are shown. The ratio between the numerical peak time and the analytic model prediction (equation 45) is between 0.8 and 1.1.

Our results highlight the difficulty in constraining the progenitor properties from current observations at a single band. The resolution of observations makes it hard to determine accurately the time of the exact peak, and even an error of 0.1 – 0.2 mag in the peak magnitude can lead to an error of 50% in the estimation of R_* . However, since the temperature evolves significantly before the peak, and its value at the peak depends only on the observed band, spectral or multi-wavelength observations can be used to significantly improve the constraints.

6.2 The breakout pulse

As discussed in sub-section 4.3, light travel time affects the emission during the breakout pulse. Figure 22 shows the rise of the R-, g - and near-UV bands. The analytic model (equation 40) fits the rise very well (light travel time neglected). The emission including light travel time is composed of a rapid increase with a typical time t_0 and a slower increase with a typical time t_{Rc} .

7 THE PHOTOSPHERIC VELOCITY

Additional information can be extracted from the velocity of observed lines in early spectra. In particular, specific lines are considered as good estimators of the photospheric velocity. These are harder to identify in early spectra compared to late ones. Nevertheless, we provide here an analytic model

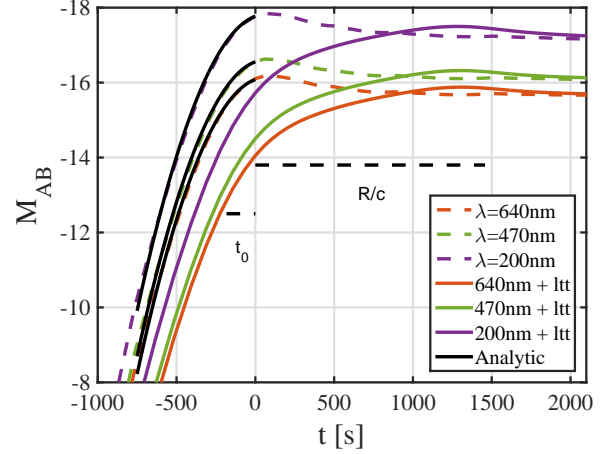


Figure 22. R-band (red line), g -band (green line) and near-UV (purple line) emission at early times, for the same numerical progenitor as used in figure 10. The numerical result with (without) light travel time is plotted in solid (dashed) lines. Including light travel time, the very early rise is of a typical time t_0 while the rise near the peak is of a typical time t_{Rc} . The analytic model (equation 40) (solid black line) is depicted in all wavelengths.

for the photospheric velocity at early times (and a comparison to the numerical results), for cases where it can be estimated before recombination becomes significant.

The position of the photosphere is determined by the point which satisfies $\tau = 1$. Since the optical depth and the shell mass, both measured from the edge of the star, are related via $\tau \approx \kappa m / 4\pi R^2$, during the planar phase the photosphere is located at $m \approx 4\pi R^2 / \kappa$. During the spherical phase, however, $R(m) \approx 2v(m)t$ (the factor of 2 is due to the rarefaction, Matzner & McKee 1999). The analytic prediction is $v(m) \propto m^{-0.12}$ (for $n = 1.5$ with weak dependency on n), which in turn yields $m_{ph} \propto t^{1.63}$. The best fit of the numerical results to a piecewise power law is similar to this analytic prediction, and is

$$\frac{m_{ph}(t)}{M_\odot} \simeq \begin{cases} 2.27 \cdot 10^{-5} R_{500}^2 & t < 1.5t_s \\ 1.45 \cdot 10^{-6} M_{15}^{-0.71} R_{500}^{-0.43} E_{51}^{0.91} t_{hr}^{1.63} & 1.5t_s \leq t \end{cases}, \quad (46)$$

and

$$\frac{R_{ph}(t)}{R_\odot} \simeq \begin{cases} R_* & t < 1.5t_s \\ 128 M_{15}^{-0.36} R_{500}^{-0.21} E_{51}^{0.45} t_{hr}^{0.81} & 1.5t_s \leq t \end{cases}. \quad (47)$$

The spherical phase of the photosphere evolution begins at $1.5t_s$ where t_s is given in equation 42. A typical evolution of R_{ph} , for the same numerical progenitor from figure 10, is depicted at the top of figure 23. The analytic model of equation 47 is compared to the numerical result, and is found to agree to within 5% during the planar and spherical phases, and to within 25% at the transition point. The results are also compared to the model of RW11 (see equation 12 therein), which yields a radius larger by about 35% during the spherical phase, relative to the calculation.

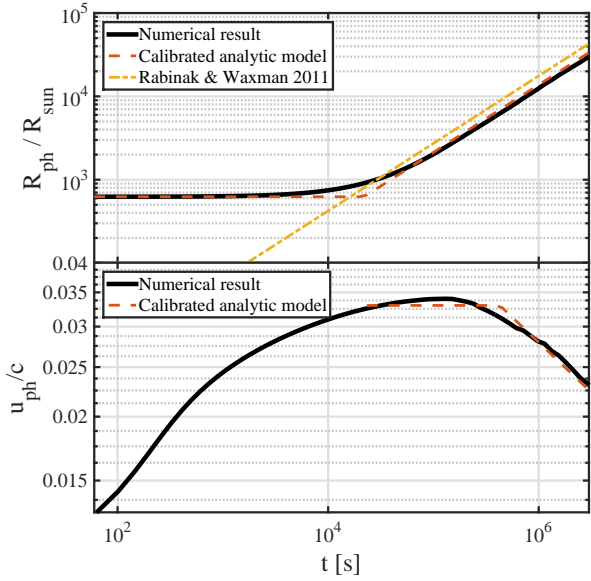


Figure 23. Top: the radius of the photosphere as a function of time from the peak luminosity, for the same numerical progenitor as used in figure 10. The numerical result (solid black line) is compared to the analytic model (equation 47, dashed red line) and to the analytic model of RW11 (dotted-dashed green line). Bottom: The velocity at the photosphere as a function of time from the peak luminosity. The numerical result (solid black line) is compared to the analytic model (equation 48, solid red line).

The numerical photosphere velocity is shown at the bottom of figure 23. The photosphere accelerates during the whole planar phase. At the beginning of the spherical phase, while the photosphere is still in the breakout shell, the velocity profile $v(m) \approx 2v_0$ is about constant (and accelerates slowly with time). Therefore, u_{ph} is almost constant. As soon as $m_{ph}(t) \geq m_0$, the velocity profile is well approximated by $v(m) = m^{-0.12}$ and $u_{ph} \propto t^{0.2}$. Again, the best fit to the numerical results is similar to the analytic prediction:

$$\frac{u_{ph}(t)}{\text{1km/s}} \simeq \begin{cases} 9 \cdot 10^3 M_{15}^{-0.44} R_{500}^{-0.49} E_{51}^{0.56} & 1.5t_s < t < t_m \\ 1.2 \cdot 10^4 M_{15}^{-0.3} R_{500}^{-0.14} E_{51}^{0.38} t_{\text{day}}^{-0.2} & t_m \leq t \end{cases} \quad (48)$$

Here, t_m is the time for which $m_{ph}(t_m) = m_0$:

$$t_m = 4.5 \text{ day } M_{15}^{0.71} R_{500}^{1.79} E_{51}^{-0.9} \quad (49)$$

This model fits the position and velocity of the photosphere to within 15% accuracy (except for the transition point around $t = t_m$) for all the numerical progenitors.

8 SUMMARY

We have studied the emission from a SN generated by the core-collapse of a RSG during the first 10 – 20 days after first light, when recombination is negligible, and the light curve is mainly determined by the thermal energy distribution at the outer envelope. We used a 1D hydro-radiation

code to simulate early light curves from explosions of different RSG progenitors, and combined analytic estimates with the numerical results to obtain an accurate analytic model for the emission. We first studied the effect of each of the SN properties R_* , M_{ej} and E_{exp} independently by defining an analytic prototype progenitor profile, and varying each parameter separately over a wide range of values. Then, we simulated the explosions of 124 RSG progenitors calculated using the stellar evolution code MESA. The numerically calculated progenitors are more realistic and have different profiles but the effect of R_* and M_{ej} cannot be studied independently over a large range of values.

First, we found that earlier analytic works deviate from the numerical results by a factor of 2–4 describing the bolometric luminosity and the features of the light curve, and by up to 50% describing the observed temperature. This deviation is mostly due to the approximations made regarding the hydrodynamic evolution of the explosion, the initial progenitor density profile and the opacity of the matter. Then, we constructed a new calibrated analytic model which describes the light curve as a function of the breakout shell properties (v_0 , ρ_0 and R_*) and as a function of the progenitor properties (M_{ej} and R_*) and explosion energy. Our model is analytic, hence the dependency on each parameter is clearly understood, yet it has the advantage of being accurate, since it was calibrated by numerical simulations where most of the assumptions and approximations made in previous analytic models are relaxed.

We found that the dependency of the light curve on the breakout shell properties is of a global nature. Progenitors with very different internal structures but the same breakout parameters produce almost identical light curves during the first day and show only minor deviation at later times. This is because during the first day (up to the spherical phase) only emission from the breakout shell is observed. Later, during the spherical phase, inner parts of the progenitor are observed but the dependence of the emission on the exact structure is mild. Thus, the early light curves directly probe mostly the properties of the breakout shell. Our model relates the bolometric luminosity to the breakout shell properties within an accuracy of 15% during the first day and at an accuracy of 25% at later times. The observed temperature is predicted by the analytic model within an accuracy of about 10% at all times. The early light curve is especially sensitive to v_0 and R_* , therefore these are the two parameters that can be most easily extracted from an early observation. The value of ρ_0 strongly affects only the timescale of the rise of the breakout emission (typically of order of minutes), therefore its value can not be well constrained without a detailed observation of the rise.

Global properties such as the ejecta mass and the explosion energy are not probed directly, but through their relation to the breakout properties. Since the mapping between E_{exp} , M_{ej} and R_* and the breakout parameters depends on the progenitor structure, the relations that we provide between the early light curve and E_{exp} , M_{ej} and R_* are less accurate than the relations with the breakout parameter. They are also less general since they depend on the specific set of numerically calculated progenitors that we explored. Our model relates the bolometric luminosity to the progenitor and explosion properties within an accuracy of

25% during the first day and 35% at later times. The observed temperature is described to within 15% accuracy.

We also derived an analytic approximation for the deviation of the observed spectrum from blackbody, mainly at the Rayleigh-Jeans regime. The source of this deviation is the higher absorption opacity at lower frequencies. As a result, photons with different frequencies are generated in different locations within the outflow, as less energetic photons are generated at outer locations where the electrons are colder. We show that over a limited range of frequencies below the spectral peak ($h\nu < k_B T_{\text{obs}}$), which for typical parameters includes the UV and optical bands, the spectrum can be approximated as $L_\nu \propto \nu^{1.4}$. This deviation has a significant effect on the optical/UV light curve during the first day, when $T_{\text{obs}} \gg 10^4$ °K, and a lesser effect at later times.

We used our results to derive and explore optical and near-UV light curves. Similarly to previous analytic (NS10) and numerical (Tominaga et al. 2011) results, the optical light curves depict two peaks. The first one corresponds to the breakout pulse (time scale of R_*/c) and is less prominent than predicted by NS10. The second (time scales of days) is the one observed in many SNe (e.g., Anderson et al. 2014; González-Gaitán et al. 2015; Gall et al. 2015; Rubin et al. 2015) and corresponds to the passage of the spectral peak through the observed band. The shape of the UV light curve, however, is different than previously predicted. Only the first peak (time scale of R_*/c) is observed, and followed by a very slow decline for several days, which turns into a very fast decline when the spectral peak drops below the observed UV band.

The time of the second optical peak was recently used to constrain the progenitor radius (González-Gaitán et al. 2015; see however Rubin et al. 2015). We found a relation between the time of this peak and the global SN parameters, and showed that it is most sensitive to the progenitor radius, in agreement with previous studies (e.g., NS10, RW11, Tominaga et al. 2011). However, we showed that deriving constraints from the time of the peak in a single band observation is very sensitive to the exact identification of its location. For example, identifying the peak at the time that the flux is only 0.1 – 0.2 mag fainter than the actual peak can lead an error of about 50% in the estimation of R_* . This highlights the difficulty in constraining progenitor properties from current observations at a single band. We also examined T_{obs} at the time of the peak and found that it is higher, but not by much, than the recombination temperature. T_{obs} vary rapidly near the peak, and it is higher than at the peak, by about 25% [40%], when the optical luminosity is only 0.1 [0.2] mag fainter than the peak. This shows that much better constraints on the SN properties can be obtained with an information about the temperature near the peak (e.g., via multi-band observations).

To conclude, we present an accurate analytic model for the early emission of type II SNe that can be used for analyzing large data sets, planning future observations, or constraining progenitor properties from a given observation. Light curves generated using our calibrated model can be downloaded at <http://www.astro.tau.ac.il/~tomersh/>.

ACKNOWLEDGEMENTS

We are grateful to Nir Sapir for stimulating discussions, and to Sivan Ginzburg for his helpful advice regarding the numerical simulation. TS and EN were partially supported by an ERC starting grant (GRB/SN), ISF grant (1277/13) and an ISA grant.

REFERENCES

- Anderson J. P., et al., 2014, *ApJ*, **786**, 67
 Arcavi I., et al., 2012, *ApJ*, **756**, L30
 Blinnikov S. I., Eastman R., Bartunov O. S., Popolitov V. A., Woosley S. E., 1998, *ApJ*, **496**, 454
 Chevalier R. A., 1976, *ApJ*, **207**, 872
 Chevalier R. A., 1982, *ApJ*, **258**, 790
 Chevalier R. A., 1992, *ApJ*, **394**, 599
 Colgate S. A., 1974, *ApJ*, **187**, 333
 Dessart L., Hillier D. J., Waldman R., Livne E., 2013, *MNRAS*, **433**, 1745
 Elliott L. A., 1960, *Proceedings of the Royal Society of London A: Mathematical*, **258**, 287
 Ensmann L., Burrows A., 1992, *ApJ*, **393**, 742
 Falk S. W., 1978, *ApJ*, **225**, L133
 Faran T., et al., 2014, *MNRAS*, **442**, 844
 Gall E. E. E., et al., 2015, *A&A*, **582**, A3
 Gezari S., et al., 2008, *ApJ*, **683**, L131
 Ginzburg S., Balberg S., 2012, *ApJ*, **757**, 178
 Glebbeek E., Gaburov E., de Mink S. E., Pols O. R., Portegies Zwart S. F., 2009, *A&A*, **497**, 255
 González-Gaitán S., et al., 2015, *MNRAS*, **451**, 2212
 Grassberg E. K., Imshennik V. S., Nadyozhin D. K., 1971, *Ap&SS*, **10**, 28
 Imshennik V. S., Nadezhin D. K., Utrobin V. P., 1981, *Ap&SS*, **78**, 105
 Katz B., Budnik R., Waxman E., 2010, *ApJ*, **716**, 781
 Katz B., Sapir N., Waxman E., 2012, *ApJ*, **747**, 147
 Magee N. H., et al., 1995, in Adelman S. J., Wiese W. L., eds, *Astronomical Society of the Pacific Conference Series Vol. 78, Astrophysical Applications of Powerful New Databases*. p. 51
 Matzner C. D., McKee C. F., 1999, *ApJ*, **510**, 379
 Mihalas D., Mihalas B. W., 1984, *Foundations of Radiation Hydrodynamics*. ed. B. W. Mihalas and D. Mihalas
 Morozova V., Piro A. L., Renzo M., Ott C. D., 2016, preprint, ([arXiv:1603.08530](https://arxiv.org/abs/1603.08530))
 Nakar E., Sari R., 2010, *ApJ*, **725**, 904
 Nieuwenhuijzen H., de Jager C., 1990, *A&A*, **231**, 134
 Nugis T., Lamers H. J. G. L. M., 2000, *A&A*, **360**, 227
 Paxton B., Bildsten L., Dotter A., Herwig F., Lesaffre P., Timmes F., 2011, *ApJS*, **192**, 3
 Paxton B., et al., 2013, *ApJS*, **208**, 4
 Paxton B., et al., 2015, *ApJS*, **220**, 15
 Piro A. L., Chang P., Weinberg N. N., 2010, *ApJ*, **708**, 598
 Pomranig G. C., 2005, *The Equations of Radiation Hydrodynamics*. Dover Publications, INC
 Rabinak I., Waxman E., 2011, *ApJ*, **728**, 63
 Richtmyer R. D., Morton K. W., 1967, *Difference Methods for Initial-Value Problems*, 2 edn. Interscience Publishers
 Rubin A., et al., 2015, preprint, ([arXiv:1512.00733](https://arxiv.org/abs/1512.00733))
 Sakurai A., 1960, *Communications on Pure and Applied Mathematics*, **13**, 353
 Sanders N. E., et al., 2015, *ApJ*, **799**, 208
 Sapir N., Halbertal D., 2014, *ApJ*, **796**, 145
 Sapir N., Waxman E., 2016, preprint, ([arXiv:1607.03700](https://arxiv.org/abs/1607.03700))
 Sapir N., Katz B., Waxman E., 2011, *ApJ*, **742**, 36
 Schawinski K., et al., 2008, *Science*, **321**, 223

- Sedov L. I., 1959, *Similarity and Dimensional Methods in Mechanics*. ed. L. I. Sedov
- Shigeyama T., Nomoto K., Hashimoto M., 1988, *A&A*, **196**, 141
- Smartt S. J., 2009, *ARA&A*, **47**, 63
- Taylor G., 1950, *Royal Society of London Proceedings Series A*, 251
- Tominaga N., Blinnikov S., Baklanov P., Morokuma T., Nomoto K., Suzuki T., 2009, *ApJ*, **705**, L10
- Tominaga N., Morokuma T., Blinnikov S. I., Baklanov P., Sorokina E. I., Nomoto K., 2011, *ApJS*, **193**, 20
- Vink J. S., de Koter A., Lamers H. J. G. L. M., 2001, *A&A*, **369**, 574
- Weaver T. A., 1976, *ApJS*, **32**, 233
- Woosley S. E., 1988, *ApJ*, **330**, 218
- Zel'dovich Y. B., Raizer Y. P., 1967, *Physics of Shock Waves and High-Temperature Hydrodynamic Phenomena*, 2 edn. Academic Press Inc.
- von Neumann J., Richtmyer R. D., 1960, *Communications on Pure and Applied Mathematics*, **13**, 353

APPENDIX A: THE HYDRO RADIATION CODE

We have written a 1D spherical geometry, Two-Temperatures Lagrangian computer program in order to calculate the shock propagation and emitted radiation after the shock breakout. The code uses the standard von Neumann and Richtmyer staggered-mesh method to solve the equations of motion (von Neumann & Richtmyer 1960; Richtmyer & Morton 1967):

$$\frac{1}{\rho} \frac{\partial \rho}{\partial t} = \vec{\nabla} \cdot \mathbf{u}, \quad (\text{A1a})$$

$$\frac{\partial \mathbf{u}}{\partial t} = -\frac{\vec{\nabla} P}{\rho} - \frac{\vec{\nabla} U_r}{3/\rho}. \quad (\text{A1b})$$

The two equations describing the radiation and matter energy densities, are

$$\frac{\partial e}{\partial t} + (P + e) \vec{\nabla} \cdot \mathbf{u} = c \kappa_P \rho (U_r - a_{\text{BB}} T_e^4), \quad (\text{A2a})$$

$$\frac{\partial U_r}{\partial t} + \left(\frac{4}{3} U_r\right) \vec{\nabla} \cdot \mathbf{u} = -c \kappa_P \rho (U_r - a_{\text{BB}} T_e^4) - \frac{\partial J}{\partial x}, \quad (\text{A2b})$$

where, U_r is the radiation energy density, e is the matter energy density, P is the matter pressure, T_e is its temperature, κ_P is Planck averaged opacity (only absorption terms are taken into account), and J is the radiation flux, which is solved under the $P0$ diffusion approximation (Richtmyer & Morton 1967; Mihalas & Mihalas 1984; Pomraning 2005):

$$J = -\frac{c}{3\kappa_R \rho} \frac{\partial U_r}{\partial x}. \quad (\text{A3})$$

Here, κ_R is the Rosseland averaged opacity. For the equation of state (EOS) of the matter, we choose that of an ideal gas, with $\gamma = 5/3$, suitable for monoatomic gas, and $\mu = 0.6$ which corresponds to a fully ionized mixture of hydrogen and helium with primordial ratios. Planck opacity includes hydrogen free-free and bound-free interactions assuming primordial ratios, and Rosseland opacity includes free-free and bound-free interactions, in addition to the scattering term $\kappa_R = 0.34 \text{ cm}^2/\text{g}$ which corresponds to Thomson opacity of

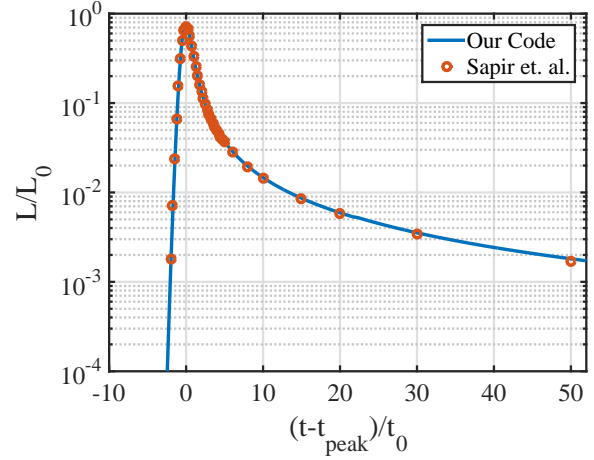


Figure A1. Normalized bolometric luminosity as a function of normalized time, for the planar shock breakout problem with $n = 1.5$ (see Sapir et al. 2011; Ginzburg & Balberg 2012). The results from our code (solid blue line) fit the results from table 3 in Sapir et al. (2011) to within 1% accuracy.

hydrogen and helium with primordial ratios. The assumptions for the opacities and EOS are reasonable as long as hydrogen is completely ionized. Therefore, our solution is limited for temperatures higher than about 7500°K .

The energy equations are solved using operator splitting. First, only the hydrodynamic part is solved implicitly for both the matter and energy equations. Then, the coupling term is solved in the method described by Sapir & Halbertal (2014), which assures energy is conserved to numerical precision. In the last step, energy diffusion is calculated implicitly, solving a tri-diagonal equation system (Richtmyer & Morton 1967; Mihalas & Mihalas 1984).

The explosion is simulated by artificially injecting thermal energy E_{exp} into the innermost cells as an initial condition. The flux boundary condition on the outermost cell, which is also used to determine the bolometric luminosity, is of an Eddington factor $f = 0.5$ (Pomraning 2005) which is equivalent to Marshak boundary condition (Zel'dovich & Raizer 1967). Since the luminosity is determined at the point $\tau \simeq c/v$, the details of the boundary condition barely affect the emission.

The code was validated via several analytic test problems, such as Elliott's extension to the Sedov-Taylor explosion which includes radiative flux (Elliott 1960) and Chevalier's solution for self-similar interaction of ejecta and wind (Chevalier 1982), and reproduced the analytic results within numerical precision. Here, in addition, we compare our results for the planar shock breakout with previous numerical calculations.

The breakout of a shock from a stellar edge in planar geometry was investigated and solved analytically by Sakurai (1960). The medium is assumed to be of ideal gas with decreasing density $\rho(x) \propto x^n$ with x the distance from the edge. Sapir et al. (2011) studied an extension to the problem which includes radiative flux, in the diffusion approximation. They assumed radiation dominated gas ($\gamma = 4/3$) and constant opacity, and numerically calculated a self-similar light curve emitted during the shock breakout and expansion. We

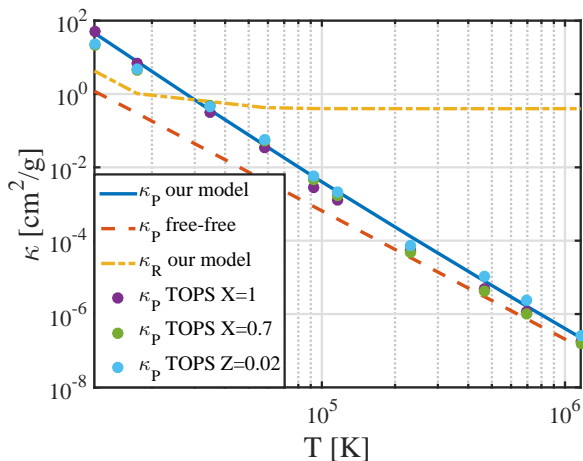


Figure B1. The opacity of different models as a function of temperature, for a typical density $\rho = 10^{-10}$ g/cc. The density used throughout this work for the determination of the observed temperature (solid blue line) is the Planck averaged opacity of hydrogen bound-free and free-free transitions. Planck opacity of free-free only (dashed red line) and Rosseland opacity of Thomson scattering, bound-free and free-free (dashed orange line) are plotted for comparison. In addition, bound-free and free-free Planck opacities, obtained from TOPS database, are shown for pure hydrogen (purple circles), hydrogen and helium with primordial ratios (green circles) and solar metallicity (cyan circles).

use this problem as a test case for our code, and compare the light curve to Sapir et al. (2011).

The calculation is performed in a method similar to the one described by Ginzburg & Balberg (2012). We use planar geometry, assume full coupling between radiation and matter, insert the appropriate density profile (with $n = 1.5$) and keep only the radiation terms of the EOS. In order to simulate the explosion, we deposited thermal energy into the innermost cell as an initial condition. In figure A1 we present the comparison of our results with the results of Sapir et al. (2011). An agreement to within 1% is found for all times. Our light curve was normalized to the breakout values t_0 and L_0 as described in Sapir et al. (2011).

APPENDIX B: BOUND-FREE AND FREE-FREE PLANCK AND ROSSELAND MEAN OPACITIES BEFORE RECOMBINATION

In the gray (P0) diffusion approximation (see appendix A), radiation-matter coupling is dependent on the Planck averaged absorption opacity, while the diffusion term contains the Rosseland averaged opacity, which includes both absorption and scattering processes (Pomraning 2005). In the expanding SN envelope, the absorption term is usually much smaller than the scattering term, thus the absorption opacity barely affects the bolometric luminosity (total energy flux). Nevertheless, since the absorption opacity dominates the coupling, it largely affects the observed temperature.

Previous studies of the emission approximated the absorption opacity as hydrogen free-free dominated (e.g. NS10). In our model, we also include bound-free transitions,

by approximating the cross section of each of the lowest 100 energy levels. The exact method of approximation is specified in Zel'dovich & Raizer (1967) chapters (V.1.3-5).

In figure B1 the Planck opacity of our model is shown for various temperatures, and density $\rho = 10^{-10}$ g/cc (since both free-free and bound-free terms are proportional to ρ^2 , our analysis applies for a wide range of densities [$10^{-12} - 10^{-9}$ g/cc]). For comparison, the free-free term of our model, and tables from TOPS database (Magee et al. 1995) for different mixtures are also shown. The mixtures which appear are pure hydrogen, hydrogen and helium with primordial ratios, and solar metallicity. In TOPS opacities, only bound-free and free-free transitions are considered, by artificially removing narrow lines. At breakout temperatures ($T_{\text{obs},0} \approx 1 - 5 \cdot 10^5$ °K) the bound-free term and the free-free term are comparable, while for lower temperatures this factor grows to more than an order of magnitude, since more photons have typical energies of the lower energy levels. For all the temperatures, the TOPS opacity changes by less than a factor of 2 between mixtures, and is similar to our model.

We deduce that the hydrogen bound-free term determines the coupling. Since $\eta_0 \propto 1/\dot{n}$ is inversely proportional to Planck opacity, and $T_{\text{obs}} \propto \eta_0^{0.07}$ (equation 8), inclusion of bound-free and free-free transitions from helium and metals changes the observed temperature by less than 5%. Neglecting hydrogen bound-free transitions, however, results in temperatures higher by 20%.

Figure B1 also depicts Rosseland opacity used in our model. For high enough temperatures, Thomson scattering indeed dominates the opacity, but at $T \approx 1 \cdot 10^4$ °K bound-free dominates. However, since Thomson scattering is density independent, and since at late times the density is much lower than $\rho = 10^{-10}$ g/cc, usually the scattering term is larger than the absorption term.

APPENDIX C: PROPERTIES OF THE NUMERICAL PROGENITORS

This paper has been typeset from a $\text{\TeX}/\text{\LaTeX}$ file prepared by the author.

Table C1. MESA calculated progenitors (part 1)

M_{ZAMS} [M_{\odot}]	Z	mixing length parameter	rotation [breakup]	M_{final} [M_{\odot}]	M_{ej} [M_{\odot}]	M_{env} [M_{\odot}]	R_{*} [R_{\odot}]
11	0.02	2	0.4	10.07	9.72	7.19	518
12	0.0002	1.5	0	12.94	11.39	8.82	608
12	0.0002	1.5	0.2	12.89	11.27	8.72	603
12	0.0002	2	0	12.93	11.31	8.80	553
12	0.0002	2	0.2	12.88	11.28	8.68	552
12	0.0002	2	0.4	12.89	11.19	8.25	609
12	0.0002	3	0	12.94	11.31	8.85	480
12	0.0002	3	0.2	12.93	11.25	8.54	512
12	0.0002	3	0.4	12.89	11.25	8.46	511
12	0.002	1.5	0	11.59	10.02	7.70	736
12	0.002	1.5	0.2	10.49	8.86	5.94	867
12	0.002	1.5	0.4	10.80	9.17	6.60	783
12	0.002	2	0	12.23	10.59	8.20	614
12	0.002	2	0.2	11.60	9.94	7.49	633
12	0.002	2	0.4	11.32	9.64	6.86	681
12	0.002	3	0	12.48	10.85	8.47	489
12	0.002	3	0.2	11.98	10.41	7.85	502
12	0.002	3	0.4	11.25	9.60	6.89	532
12	0.002	5	0	12.66	11.02	8.72	396
12	0.002	5	0.2	11.48	9.86	7.12	438
12	0.002	5	0.4	12.23	10.65	7.90	432
12	0.02	1.5	0	11.51	9.97	7.93	910
12	0.02	1.5	0.2	11.36	9.93	7.74	926
12	0.02	1.5	0.4	11.16	9.59	7.45	948
12	0.02	1.5	0.6	9.93	8.26	5.52	1052
12	0.02	2	0	11.70	10.07	8.08	709
12	0.02	2	0.2	11.49	9.92	7.84	752
12	0.02	2	0.4	11.23	9.65	7.48	778
12	0.02	2	0.6	10.29	8.65	5.84	841
12	0.02	3	0	11.92	10.34	8.36	559
12	0.02	3	0.2	11.86	10.27	8.23	568
12	0.02	3	0.4	11.41	9.81	7.60	592
12	0.02	3	0.6	11.19	9.53	6.78	650
12	0.02	5	0	12.27	10.70	8.70	383
12	0.02	5	0.2	11.87	10.31	8.19	388
12	0.02	5	0.4	11.78	10.16	8.11	390
12	0.02	5	0.6	11.00	9.27	6.66	445
12	0.02	5	0.8	10.08	8.27	4.87	510
13	0.02	2	0	11.71	10.00	8.11	708
13	0.02	2	0.2	11.56	9.95	7.91	711
13	0.02	2	0.4	11.26	9.53	7.48	739
13	0.02	2	0.6	10.01	8.18	5.50	847
14	0.02	2	0	12.34	10.68	8.33	780
14	0.02	2	0.2	12.04	10.28	7.89	817
15	2e-05	1.5	0	14.98	13.27	10.29	555
15	2e-05	1.5	0.4	14.76	12.74	9.40	601
15	2e-05	3	0	14.97	13.07	10.18	465
15	2e-05	3	0.4	14.91	12.77	9.59	496
15	2e-05	5	0	14.98	13.22	10.30	390
15	2e-05	5	0.4	14.90	12.85	9.35	442
15	0.0002	1.5	0	14.95	13.10	10.13	608
15	0.0002	1.5	0.4	14.77	12.70	9.40	658
15	0.0002	3	0	14.92	13.02	10.02	476
15	0.0002	3	0.4	14.83	12.79	9.29	524
15	0.0002	5	0	14.93	13.16	10.14	394
15	0.0002	5	0.4	14.79	12.60	9.27	448
15	0.002	1.5	0	14.27	12.53	9.56	778
15	0.002	1.5	0.4	10.37	8.62	5.18	894
15	0.002	3	0	14.10	12.21	9.28	518
15	0.002	3	0.4	12.62	10.58	7.41	562
15	0.002	5	0	14.44	12.68	9.69	401
15	0.002	5	0.4	13.63	11.79	8.45	432

Table C2. MESA calculated progenitors (part 2)

M_{ZAMS} [M_{\odot}]	Z	mixing length parameter	rotation [breakup]	M_{final} [M_{\odot}]	M_{ej} [M_{\odot}]	M_{env} [M_{\odot}]	R_{*} [R_{\odot}]
15	0.02	2	0	13.05	11.27	8.68	835
15	0.02	2	0.2	12.66	10.94	8.17	841
15	0.02	2	0.4	13.15	11.37	8.60	845
16	0.02	2	0	14.47	12.68	9.67	851
16	0.02	2	0.2	13.25	11.47	8.38	883
16	0.02	2	0.4	12.71	10.78	7.66	943
17	0.02	2	0	14.25	12.47	9.10	963
17	0.02	2	0.2	13.44	11.59	8.07	977
17	0.02	2	0.4	13.19	11.25	7.73	1009
18	0.02	2	0	16.25	14.23	10.67	978
18	0.02	2	0.2	15.22	13.32	9.61	1015
18	0.02	2	0.4	13.89	11.93	8.06	1031
19	0.02	2	0	15.46	13.53	9.58	1046
19	0.02	2	0.2	14.47	12.50	8.34	1077
20	2e-05	3	0.4	17.88	17.17	10.91	666
20	0.0002	1.5	0	19.94	17.41	13.33	471
20	0.0002	1.5	0.4	19.48	16.86	11.38	812
20	0.0002	3	0	19.91	17.90	12.93	616
20	0.0002	3	0.4	19.45	16.76	11.12	680
20	0.0002	5	0	19.92	17.57	13.11	511
20	0.0002	5	0.4	19.38	16.76	11.02	561
20	0.002	1.5	0	14.69	12.62	7.83	1027
20	0.002	1.5	0.4	12.73	10.59	5.18	991
20	0.002	3	0	15.70	13.67	8.65	703
20	0.002	3	0.4	14.72	12.44	7.04	735
20	0.002	5	0	16.70	14.69	9.94	529
20	0.02	2	0	15.41	13.38	9.11	1025
20	0.02	2	0.2	15.00	13.02	8.63	1019
21	0.02	2	0	15.74	13.70	9.04	1037
21	0.02	2	0.2	14.98	12.95	8.26	1030
21	0.02	2	0.4	11.47	9.18	4.43	925
22	0.02	2	0	17.37	15.01	10.36	1039
22	0.02	2	0.4	12.31	10.23	4.88	945
23	0.02	2	0	16.80	14.70	9.40	1032
23	0.02	2	0.2	13.09	11.04	5.60	986
23	0.02	2	0.4	12.94	10.80	5.13	942
24	0.02	2	0	16.32	14.22	8.47	1040
24	0.02	2	0.2	14.63	12.55	6.75	1005
25	2e-05	1.5	0	24.97	22.17	16.01	154
25	2e-05	1.5	0.4	19.00	15.87	7.78	1018
25	0.0002	3	0.4	18.33	15.18	7.53	784
25	0.0002	5	0	24.90	22.58	15.95	149
25	0.0002	5	0.4	16.20	13.22	5.38	639
25	0.002	1.5	0	14.30	11.63	5.21	994
25	0.002	1.5	0.4	20.00	17.31	10.06	1030
25	0.002	3	0	17.94	15.31	8.78	799
25	0.002	3	0.4	19.40	16.51	9.39	756
25	0.002	5	0	18.44	16.22	9.29	646
25	0.002	5	0.4	20.54	17.79	10.83	640
25	0.02	2	0	16.08	13.89	7.86	1016
25	0.02	2	0.2	13.62	11.46	5.34	950
26	0.02	2	0	16.45	14.10	7.79	943
26	0.02	2	0.2	13.88	11.49	5.22	900
27	0.02	2	0	16.22	13.38	7.14	917
27	0.02	2	0.2	13.37	10.61	4.28	811
28	0.02	2	0	15.66	12.81	6.12	844
28	0.02	2	0.2	19.53	16.63	10.24	902
29	0.02	2	0	16.21	13.40	6.25	790
30	0.02	2	0	16.05	13.37	5.62	703
30	0.02	2	0.2	15.34	12.52	5.04	697
35	0.02	2	0	17.11	14.47	4.55	377
35	0.02	2	0.2	17.10	14.37	4.55	380